Journal of Geoscience and Environment Protection, 2025, 13(9), 75-107
https://www.scirp.org/journal/gep
ISSN Online: 2327-4344
ISSN Print: 2327-4336

Mineralogical, Petrological, and Geochemical Features of Alkali Basalts from the Dibi Area, Adamawa Plateau (Cameroon Volcanic Line)

Paterne Mulimbi Kagarabi[1,2], Boris Chako-Tchamabe[3], Jules Tamen[1], Kaniki Tumba[4], David G. Nkouathio[1], Theodoros Ntaflos[5], Lowanika Victor Tibane[6], Charles Nzolang[2], Synthia Nguimatsia Tengomo[1]

[1]Department of Earth Sciences, Faculty of Science, University of Dschang, Dschang, Cameroon
[2]Filière de Géologie, Domaine des Sciences et Technologie, Université Officielle de Bukavu, Bukavu, Democratic Republic of the Congo
[3]Instituto de Investigaciones en Ciencias de la Tierra, Universidad Michoacana de San Nicolás de Hidalgo, Morelia, Mexico
[4]School of Chemical and Minerals Engineering, Faculty of Engineering, North-West University, Potchefstroom, South Africa
[5]Department of Lithospheric Research, University of Vienna, Vienna, Austria
[6]School of Agricultural, Earth and Environmental Sciences, University of KwaZulu-Natal, Durban, South Africa
Email: *mulimbi.kagarabi@uob.ac.cd

How to cite this paper: Mulimbi Kagarabi, P., Chako-Tchamabe, B., Tamen, J., Tumba, K., Nkouathio, D. G., Ntaflos, T., Tibane, L. V., Nzolang, C., & Nguimatsia Tengomo, S. (2025). Mineralogical, Petrological, and Geochemical Features of Alkali Basalts from the Dibi Area, Adamawa Plateau (Cameroon Volcanic Line). *Journal of Geoscience and Environment Protection, 13,* 75-107.
https://doi.org/10.4236/gep.2025.139005

Received: July 25, 2025
Accepted: September 13, 2025
Published: September 16, 2025

Abstract

Located southeast of the city of Ngaoundéré (Adamawa Plateau) within the continental section of the Cameroon Volcanic Line (CVL), the village of Dibi has been the scene of numerous volcanic manifestations, dominated by three types of dynamism (explosive phreatomagmatic, effusive, and Strombolian eruptions); whose rocks, however, are poorly studied. Here, the lavas emitted during those eruptions are analyzed to constrain their origin. Whole rock geochemistry revealed that these rocks consist of basanites and foidites with Mg# varying from 67.3% to 71.2%. They are porphyritic and mainly composed of olivine [($Fo_{77.28\text{-}87.28}$ in foidites) and ($Fo_{78.92\text{-}87.04}$ in basanites)], diopside [($Wo_{51}En_{35}Fs_{14}$ in foidites) and ($Wo_{50\text{-}46.18}En_{34.8\text{-}41.29}Fs_{10.41\text{-}15.92}$ in basanites)], plagioclase [(labradorite: $Ab_{37.31\text{-}39.67}An_{57.43\text{-}60.70}Or_{1.99\text{-}2.28}$) in basanites], and alkali feldspar [(anorthoclase: $Ab_{64.45\text{-}65.13}An_{6.81\text{-}9.15}Or_{26.87\text{-}27.08}$ in foidites and $Ab_{60.92\text{-}64.11}An_{8\text{-}8.47}Or_{28.45\text{-}32.27}$ in basanite)]. Accessory minerals include Al-chromite, Ferrian chromite, titanomagnetite, and apatite. The lavas are silica-undersaturated (SiO_2: 38.9 - 40.3 wt.% in foidites and SiO_2: 42.5 - 43.6 wt.% in basanites). They are within-plate basalts with similar features to Oceanic Island Basalt (OIB) magmas, affinity to High-μ (HIMU), Enriched type I (EM1), and recycled component. Their primary melts derived from low degrees of partial melting (3% - 5%) of a garnet peridotite mantle source, as shown by the Nb/La (1.30 - 1.51), Zr/La (4.91 - 5.85), and Zr/Ce (2.49 - 2.88) ratios that are consistent

with an OIB-like asthenospheric mantle source. Equilibration temperatures have been estimated from the clinopyroxene-liquid thermometer and range between 981.6˚C and 1051.6˚C, at pressures of 0.9 - 1.6 kbar.

Keywords

Cameroon Volcanic Line, Dibi, Within-Plate Basalts, OIB-Like Asthenospheric Mantle Source, High-μ

1. Introduction

Déruelle et al. (1991) and Asaah et al. (2014) reviewed early research on the Cameroon Volcanic Line (CVL) geochemistry, highlighting: 1) The origin of the CVL stems from a series of interconnected events, such as mantle plumes and lithospheric process structures; 2) CVL magmas were generated by low (<3%), but varying degrees of partial melting of a garnet lherzolite-dominated (<10%) mantle; 3) Minimal continental crustal contamination, with the magmatic evolution governed by low-degree fractional crystallization in mafic lavas and assimilation-fractional crystallization (AFC) processes during the transition from mafic to felsic compositions; 4) CVL lavas are typical of the alkaline series with all the distinct terminology of the alkaline assemblages: picrites, alkali-basalts, hawaiites, mugearites, benmoreites, phonolites, trachytes and alkali-rhyolites; 5) Mount Cameroon and the three volcanic massifs of Bioko Island are made exclusively of basaltic lava; 6) phonolites dominate the basaltic lavas in the south of Principe Island, trachytes are abundant at Mount Oku and in the Bénoué Upper Valley in Garoua, and rhyolites on the Kapsiki Plateau, whereas 7) basic and intermediate rocks have augite, titanaugite, and salite as clinopyroxene, while ferroan-augite and sodic and calci-sodic clinopyroxene are the phases found in acid rocks.

On the Adamawa plateau, where magmatism has so far been very little studied compared to the southern continental sector of the CVL, the few studies carried out show: 1) A silicic magmatism dominated by nepheline-normative trachytes which are associated with strongly alkaline basalts and basanitic rocks (Marzoli et al., 1999); 2) A degree of partial melting under 2% (Tiabou et al., 2018); 3) FOZO (Focal Zone)-type mantle and asthenospheric plume sources (Nkouandou et al., 2008; Tiabou et al., 2018); 4) Apart from the types of clinopyroxene mentioned by Déruelle et al. (1991), diopside also exists in the lavas of Adamawa (e.g., Dili-Rake et al., 2022). These data provide a general geochemical framework for the present study, allowing a more detailed comparison of lava compositions in the Adamawa Plateau and helping to refine models of mantle source variability and melt dynamics.

In this work, we present new petrographic data, whole-rock geochemistry, and the chemical composition of the minerals from a suite of volcanic rock samples collected from volcanic landforms in the locality of Dibi, southwest of the city of Ngaoundéré, Adamawa region. We reconstruct the petrogenetic processes and aim to contribute to understanding the petrology of the Adamawa Plateau.

2. Geological Setting

The Cameroon Volcanic Line is an approximately 1600 km long chain consisting of Cenozoic volcanic centers (**Figure 1**). It is a seismically active and highly faulted system (Tanyileke et al., 1996) situated above the Central Cameroon Shear Zone, a major N70 reactivated Precambrian wrench fault (Ngako et al., 1992). Along the CVL, volcanic edifices developed simultaneously in continental and oceanic settings (**Figure 1**). The continental sector includes large-volume polygenetic and small-volume volcanoes. Among the large volcanoes are Mount Etindé, Mount Cameroon, Mount Manengouba, Mount Bambouto, Mount Oku, high massifs such as Tchabal Nganha, Tchabal Djinga, and Tchabal Mbabo found in the Ngaoundéré (Adamawa) Plateau, and the Mandara Mountains found at the far northern end of the line. Smaller structures like maars, cinder cones, and short lava flows are found in monogenetic volcanic fields, known as grabens. Unlike large volcanoes, many of these smaller ones remain unnamed and lack detailed descriptions and geochemical analyses. The oceanic sector comprises six volcanoes, including the islands of Pagalu, São Tomé and Príncipe, and the three volcanoes that form Bioko Island. A comparative study of basalts between polygenetic and monogenetic volcanoes along the CVL by Sato et al. (1990) suggests that the main sources of the magmas that fed the polygenetic volcanoes originated from asthenospheric upwelling beneath the African plate, while those that fed the monogenetic eruptions resulted from partial melting in the lowermost part of the subcontinental lithosphere.

The Adamawa Plateau is a horst volcano-tectonic structure limited to the north and south, respectively, by the Adamawa and Djérem-Mbéré faults (Dumont, 1987; Dili-Rake et al., 2022). Its basement is made up of metamorphic rocks and granitoids related to the Pan-African orogeny (615 ± 27 to 652 ± 10 Ma) or earlier (880 ± 55 to 1008 ± 65 Ma) (Tchameni et al., 2006).

This plateau was the site of significant Mid-Pliocene volcanic activity (Nkouandou et al., 2008), creating high massifs such as Tchabal Djinga, Tchabal Mbabo, and Tchabal Nganha. Alkaline basalt effusive flows contributed to the formation of an irregular relief on the plateau to the north and east of Ngaoundéré (Nkouandou et al., 2010). About sixty eruptive centers, including plugs and maars, have been recorded within and around Ngaoundéré; their diversity and the variety of their products highlight the different eruptive styles reported in this area (Temdjim et al., 2006; Nkouandou et al., 2008, 2010). Geophysical studies conducted by Poudjom Djomani et al. (1995) indicate that the continental crust beneath the Adamawa is thin (23 km) and rests on an abnormally hot mantle characterized by low P-wave velocities (7.8 km/s) (Dorbath et al., 1986). The Bouguer anomaly map of west-central Africa, established by Poudjom Djomani et al. (1995), shows that the Adamawa uplift is marked by a broad, long-wavelength negative anomaly with an amplitude of −120 mGal.

Dibi is a village in a volcanic field northeast of Ngaoundéré on the Adamawa Plateau, situated at latitudes 7˚00' - 7˚07'59''N and longitudes 13˚43' - 14˚00'E, within the eastern branch of the CVL.

Dibi was the site of several eruptive manifestations at the origin of the emplacement of the volcanic products encountered. In this locality, three types of eruptive dynamism were observed:

- An explosive dynamism, linked to phreatomagmatism, is at the origin of maars (maar Mbela Guinadji, maar Gaguba, maar Ranch Ngaoundaba; **Figure 2(a)**). The main products of this dynamism are phreatomagmatic deposits (tephra and fragments of pre-existing rocks). On the slopes of the maars, fine blackish ash is found, containing granite enclaves in places (**Figure 2(b)**), millimeter- to centimeter-sized, rounded to sub-rounded basalt blocks, as well as basalt blocks and bombs of various sizes, most containing ultrabasic nodules with a diameter of less than 0.5 cm.
- Effusive activity caused lava flows that belong to the recent basaltic series of Mio-Pliocene age (10.0 to 7.0 ± 0.2 Ma and 11.39 ± 0.03 to 9.28 ± 0.03 Ma) described by Nkouandou et al. (2008).
- Strombolian activity caused the Strombolian cones present in the study area (**Figure 2(a)**). The products of this mixed activity are pyroclastics and lava flows. The pyroclastic products observed are lapilli, volcanic ash, blocks, scoria, and bombs. Most of these bombs brought back mantle and crustal xenoliths (**Figures 2(c)-(d)**).

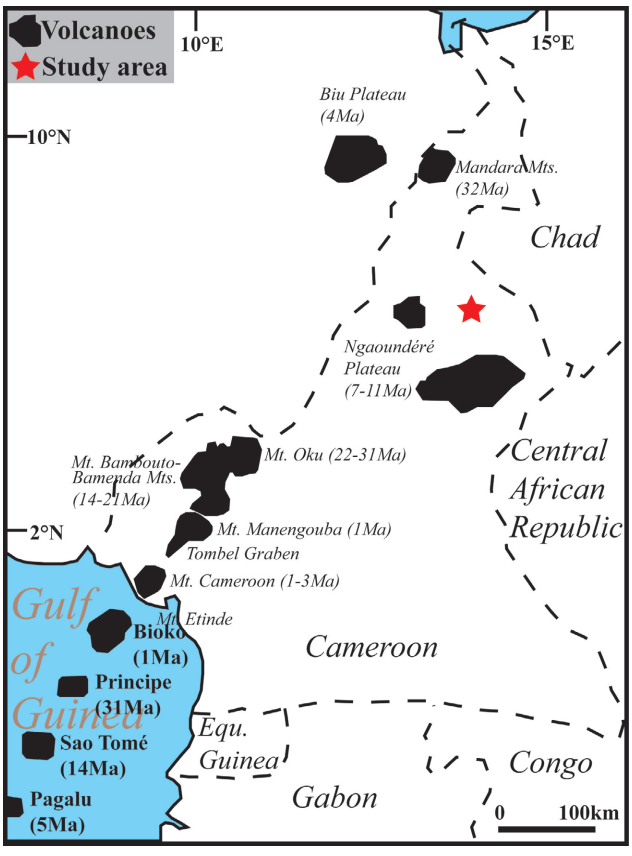

Figure 1. Distribution of The main volcanic centers within the Cameroon Volcanic Line ((Ngwa et al., 2017) modified)). Radiometric ages are from Suh et al. (2008).

3. Materials and Methods

This study focuses on the lavas sampled alongside mantle xenoliths in the village of Dibi.

Five volcanic rocks were collected for the study, including two from the Guinadji volcano (DBV5 and DBV6), one from the Mbela Guinadji maar (GBV8), and two from a plateau basalt at 13˚44'41.2"E, 7˚09'25.5"N (GBC1 and GBC2). The Guinadji volcano (longitude 13˚44'14.3"E, latitude 7˚09'11"N) culminates at 1284 m, while the Mbela Guinadji maar (longitude 13˚44'32"E, latitude 7˚09'33"N) is located at an altitude of 1187 m and occupies an area of 82737.2 m^2. The Guinadji volcano is separated from the Mbela Guinadji maar by approximately 1 km.

Samples from both the Guinadji volcano and the Mbela Guinadji maar consist of volcanic bombs 10 to 30 cm in diameter. These samples are vesicular and contain crustal and mantle xenoliths.

Collecting samples from the Mbela Guinadji maar was challenging due to the high concentration of extremely fine mantle xenocrysts (less than 2 cm), unlike samples from the Guinadji volcano, which contained crustal and mantle xenoliths with a diameter greater than 10 cm and were therefore easier to separate from the carrier lava. The two lava block samples of plateau basalts are dense and contain almost no xenocrysts or xenoliths, unlike the earlier samples. Nevertheless, to obtain representative samples with no xenocrysts or xenoliths, the fresher cores of the selected samples (volcanic bombs or lava blocks) were first crushed into fine chips of 0.5 to 1 cm and checked under a binocular stereoscopic microscope to pick out the parts with xenocrysts. These were then cleaned with distilled water, dried in the oven for 24 hours at 110˚C, and pulverized for one to two minutes per sample in a milling machine (FRITSCH brand) to obtain powder for major and trace element analysis. After each pulverization, the milling machine was cleaned using a brush, compressed air, and acetone.

Whole-rock analyses were carried out in the ALS Minerals laboratory of Johannesburg (South Africa). Major elements were analyzed through the ICP-AES method, while trace and rare earth elements were analyzed using ICP-MS. Detection limits are 0.01 wt. % for major elements, 0.01-20 ppm for trace elements, and 0.01 - 0.5 ppm for rare earth elements.

For the major elements, 200 mg of each sample powder was combined with 0.90 g of lithium metaborate/tetraborate, thoroughly mixed, and placed in a furnace at 1000˚C. The resulting liquid was cooled and dissolved in a solution of 0.4% nitric acid and 0.2% hydrochloric acid. This solution was then analyzed using ICP-AES, with the results corrected to eliminate inter-element spectral interferences. The oxide content was calculated from the determined elemental concentrations, and the results were expressed as oxide percentages. For trace elements, a 200 mg prepared sample was added to 0.90 g of lithium borate flux, mixed well, and heated in a furnace at 1000˚C. After cooling, the liquid was dissolved in a 0.4% nitric acid and 0.2% hydrochloric acid solution. The solution was then analyzed by ICP-MS, and trace and rare earth elements were reported in ppm.

The major element composition of minerals was analyzed using a Cameca SXFive FE electron microprobe at the Department of Lithospheric Research, University of Vienna, Austria. The analysis was conducted with an acceleration voltage of 15 kV and a beam current of 20 nA. Counting times included 20 seconds for peak positions and 10 seconds for background measurements. Well characterized homogeneous natural and synthetic minerals were used as standards. The average of 10 analyses during the EPMA session of the internal standard Augite ENM is given in Table 1. The standard deviation from the mean is below 0.12 and the detection limit of the measurement elements ranges from 190 to 580 ppm. The Mg-number (Mg#) and Fe-number (Fe#) refer to the atomic ratios of $Mg/(Mg + Fe^{2+})$ and $Fe^{2+}/(Fe^{2+} + Mg)$, respectively.

For this analysis, prepared thin sections were initially cleaned with water and alcohol to remove impurities and dust particles. They were subsequently placed in an ultrasonic bath with acetone for five minutes, and rinsed with ethanol. To facilitate electrical conductivity between electron-proton pairs within the crystal atoms, a carbon layer of 17 - 27 nm thickness was applied to the surface of each section. The sections were then mounted on slide holders and inserted into a vacuum chamber equipped with cameras, electron detectors, and X-ray sensors.

Table 1. Internal standard augite ENM.

Oxides in wt%	1	2	3	4	5	6	7	8	9	10	Average	STDEV
SiO_2	50.24	50.11	50.09	49.94	50.17	50.31	50.12	50.28	50.03	50.26	50.16	0.119
TiO_2	1.42	1.44	1.46	1.45	1.43	1.45	1.43	1.40	1.40	1.43	1.43	0.021
Al_2O_3	7.47	7.45	7.55	7.47	7.43	7.57	7.34	7.42	7.46	7.42	7.46	0.065
Cr_2O_3	0.01	0.00	0.00	0.00	0.00	0.00	0.00	0.00	0.01	0.00	0.00	0.005
FeO	8.26	8.33	8.25	8.25	8.29	8.16	8.20	8.24	8.33	8.27	8.26	0.053
CaO	17.35	17.34	17.34	17.51	17.47	17.36	17.47	17.40	17.33	17.31	17.39	0.071
MnO	0.12	0.15	0.14	0.13	0.15	0.15	0.14	0.13	0.13	0.13	0.14	0.008
MgO	12.36	12.27	12.15	12.29	12.39	12.35	12.31	12.17	12.25	12.47	12.30	0.098
Na_2O	2.39	2.34	2.32	2.32	2.35	2.41	2.33	2.37	2.39	2.33	2.35	0.032
Total	99.61	99.43	99.27	99.36	99.65	99.76	99.33	99.43	99.34	99.62	99.48	0.168
Det.Lim ppm	1	2	3	4	5	6	7	8	9	10	Average	
Si	252	256	250	245	249	249	245	249	239	247	248.1	
Ti	305	310	313	320	329	315	310	317	305	331	315.5	
Al	175	174	178	179	179	173	175	179	180	175	176.7	
Cr	187	191	192	188	190	192	191	190	189	192	190.2	
Fe	565	580	573	577	585	587	589	588	595	588	582.7	
Ca	352	339	345	335	352	344	350	361	343	354	347.5	
Mn	231	226	232	231	229	229	231	228	232	231	230	
Mg	227	220	234	223	209	223	234	220	218	221	222.9	
Na	256	250	246	248	238	230	244	253	237	241	244.3	

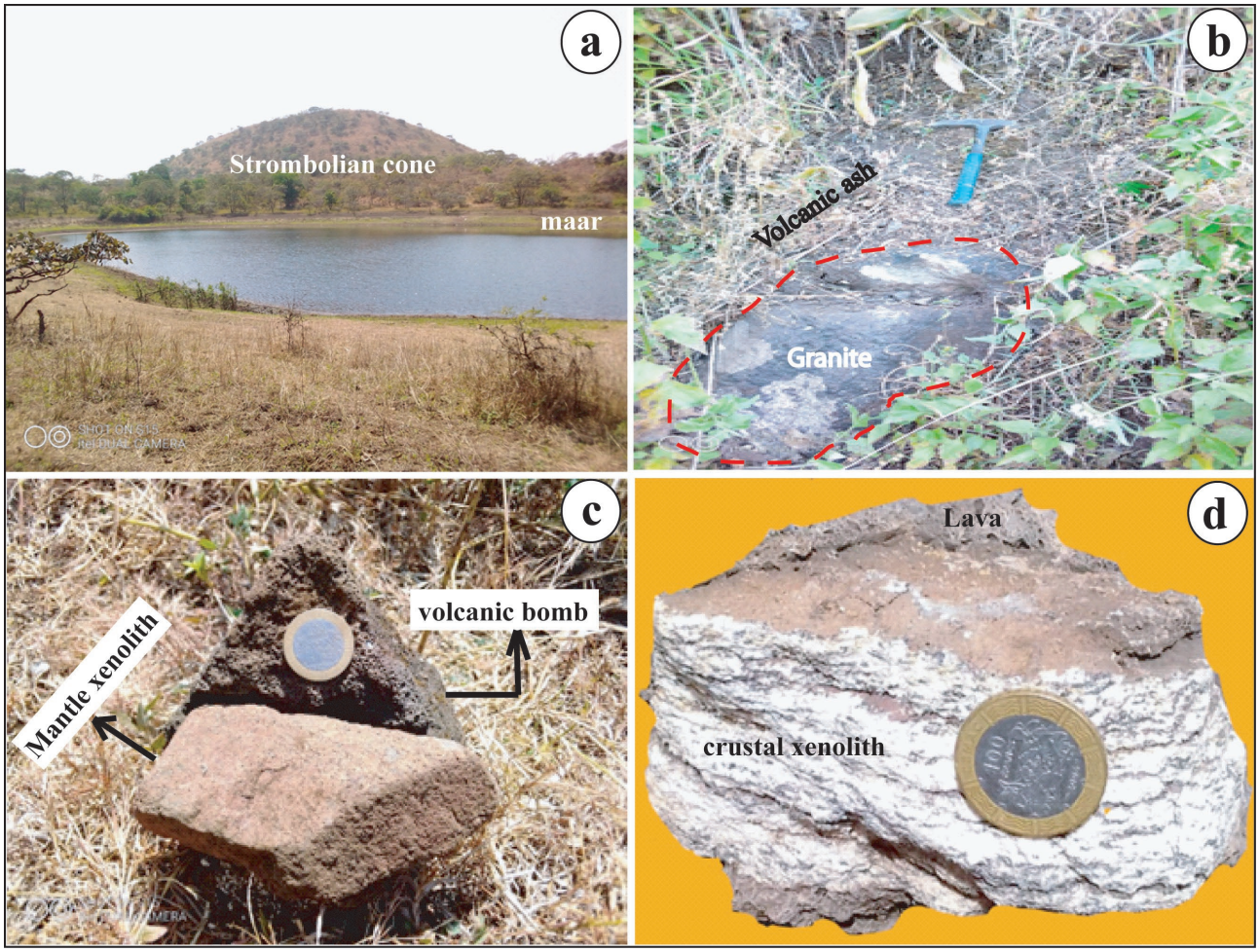

Figure 2. Field photographs of Dibi. (a) Mbela Guinadji Maar and Guinadji Strombolian cone. (b) Granite enclave in the ash on the slopes of the maar. (c) Mantle xenolith in a volcanic bomb, and (d) Crustal xenolith.

4. Results

4.1. Petrography

Macroscopically, samples from the study area are homogeneous with no clear distinction in hand specimens. The only major difference is that some are vesicular (DBV5, DBV6, and GBV8) and others are dense (GBC1 and GBC2; **Figure 3(a)-(b)**). Under the microscope, these lavas have a porphyritic microlithic texture with olivine (**Figure 3(c)**), plagioclase, and diopside phenocrysts.

Olivine occurs as euhedral to subhedral grains, sometimes unhedral, ranging in size from 0.4 to 0.5 mm. Most crystals show destabilization features. These include cracks, kink bands, inclusions of opaque minerals, and reaction crowns. Cracks are observed on crystals of different sizes. Some very cracked crystals occur as aggregates of small associated olivine crystals and sometimes show kink bands. Euhedral crystals are the least cracked and have straight grain boundaries. Reaction crowns concern only a few crystals with a size between 0.4 and 0.1 mm. These have rims with new olivine and plagioclase developing at the expense of the primary olivine, and this is achieved by leaving the rim towards the core (**Figure 3(d)**). Some crystals

have a rim corroded by glass containing opaque minerals. At the contact with the other minerals (diopside and plagioclase), no rim reaction is observed.

Diopside is subhedral, less cracked than olivine, and has a size that varies between 0.2 and 0.3 mm. The crystals are mostly elongated sections, with parallel

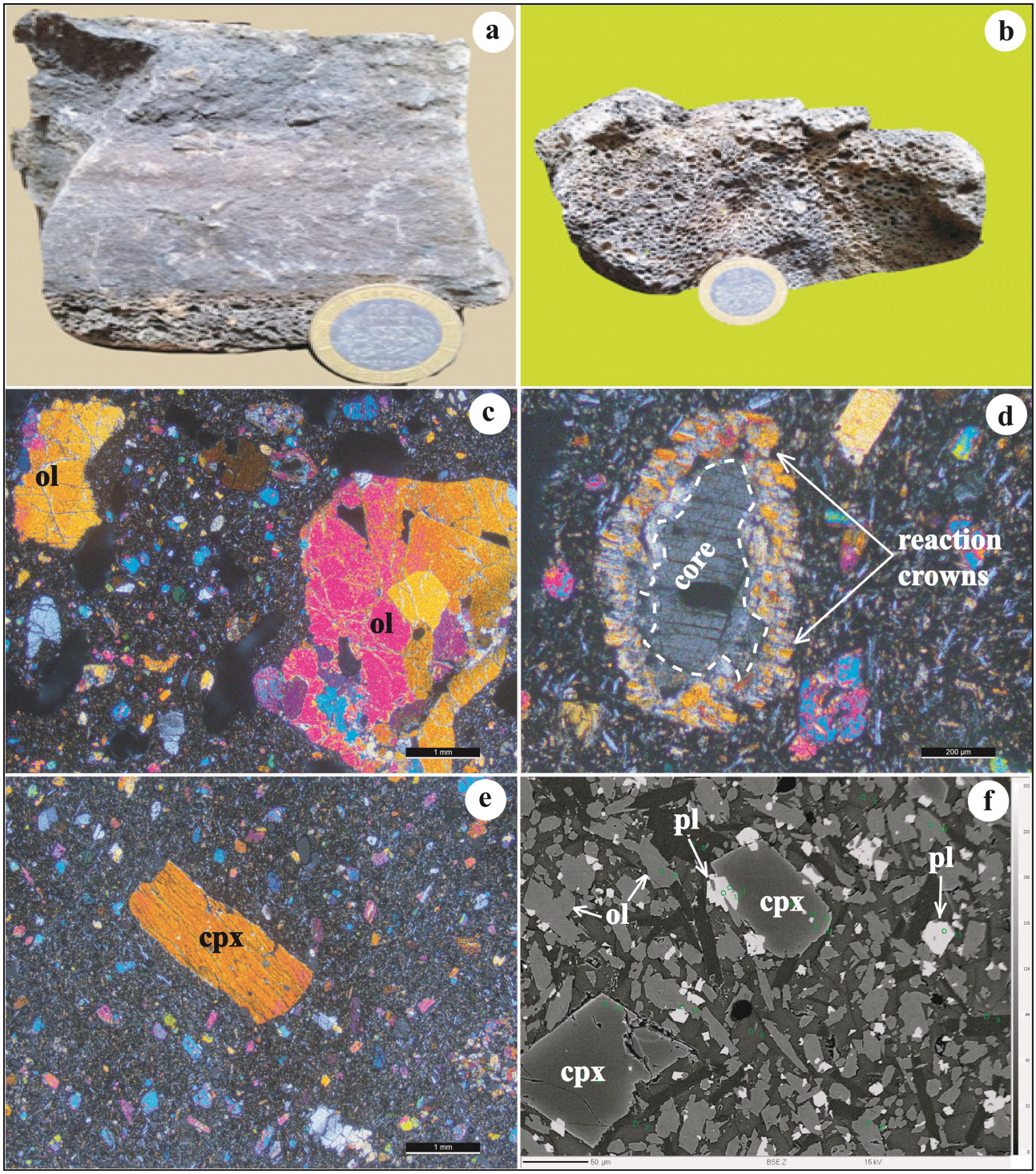

Figure 3. Photographs and microphotographs of Dibi lavas. (a) Dense lava; (b) Vesicular lava; (c) Porphyritic microlithic texture; (d) Reaction crown around olivine; (e) Elongated section of diopside; (f) BSE image of the mesostasis.

cleavages forming different angles with the crack plane (Figure 3(e)), yellowish in LPNA, with pleochroism ranging from yellow to greenish yellow. Some crystals are poikilitic, containing inclusions of opaque minerals, plagioclase, and olivine, or are sometimes corroded from the edge to the core by glass containing the same opaques. Twins are sometimes observed.

Plagioclase occurs in the form of grains measuring 0.4 to 0.1 mm. It is euhedral to subhedral. It is easily identifiable by its polysynthetic twins, which give it a striped appearance. They are occasionally in contact with diopside, showing a destabilization feature resulting in a corroded core. A type of secondary plagioclase develops, with secondary olivine replacing certain primary olivine crystals.

The mesostasis represents 45 to 55% of the thin section and is composed of diopside, olivine, plagioclase, spinel, titanomagnetite, apatite, and other opaque minerals (Figure 3(f)). Titanomagnetite is unhedral, with 20 to 40 µm in size. It is intercalated between the other mineral phases. Some grains with a size not exceeding 100 µm occur as polycrystalline aggregates at the contact of olivine and diopside. The apatite grain is sub-automorphic. It is approximately 30 to 70 µm in size. It is found either as an inclusion in the diopside or intercalated between diopside and olivine.

4.2. Whole Rock Geochemistry

4.2.1. Major Elements

The major and trace element concentrations of Dibi lavas are presented in Table 2 and Table 3. The whole-rock SiO_2 content of these lavas ranges between 38.9 and 43.6 wt.%, characteristic of ultrabasic lavas. MgO and Mg-numbers (Mg#) vary from 12.65 to 15.9 wt.% and 67.3 to 71.2, respectively. This Mg# is higher than those described at Wakwa plain (42 - 61 (Onana François Xavier et al., 2022)) and Baossi-Warack (40.05 - 64.44 (Tiabou et al., 2018)) in the Adamawa Plateau and comparable to the values assumed for primary magmas in some case studies (Mg# > 68; e.g. (Jung & Masberg, 1998)). The Al_2O_3 (11.4 - 12.45 wt.%) and CaO (9.57 - 10.5 wt.%) contents are high, with CaO/Al_2O_3 ratios ranging between 0.83 - 0.91. TiO_2 (2.62 - 3.01 wt.%) and P_2O_5 (0.67 - 0.81 wt.%) contents are low. In addition, the studied lavas have relatively medium Na_2O (1.88 - 3.16 wt.%) and low K_2O, varying from 0.85 to 1.83 wt.%, with $Na_2O + K_2O$ contents ranging from 2.73 to 4.99 wt.%. The LOI values are ≤ 1 wt.%, except in one sample with 3.06 wt.% (Table 2).

According to the TAS classification of Le Bas et al. (1986), the samples are foidites and basanites (Figure 4(a)). In the Zr/Ti versus Nb/Y diagram of (Pearce, 1996) (Figure 4(b)), the studied samples plot in the alkali basalt field and slightly fall within the transition field between alkali basalt and foidites. The samples plot in the potassic series in the Na_2O versus K_2O diagram after (Le Maitre, 2002) (Figure 4(c)), except for one basanite (GBC 2), which falls within the transition field between the potassic and sodic series. Their Na_2O/K_2O ratios vary between 1.73 and 2.21 wt.%. In the major oxides versus SiO_2 diagram (Figure 5), positive trends

in Na_2O and K_2O and slight negative trends in MgO, Fe_2O_3, TiO_2, Al_2O_3, and P_2O_5 can be deciphered. These negative trends suggest minor fractionations of olivine, Fe-Ti oxides, plagioclase, and apatite, respectively.

The major element concentrations were also used to calculate the CIPW norm (Table 2). The normative orthoclase has a higher concentration than albite, indicating the potassic nature of these rocks. Olivine (24.52% - 33.52%), nepheline (7.85% - 14.32%), and diopside (17.65% - 26.44%) are present in the Dibi rock samples, along with small amounts of apatite (1.55% - 1.88%), magnetite (2.33% - 2.51%), and ilmenite (4.98% - 5.72%). Based on these CIPW normative calculations and the classification scheme of alkali basalts proposed by (Chih, 1988), the studied lavas are plotted in the alkali picrite basalt field (Figure 4(d)), except for the sample GBC 2, which plots in the basanite field.

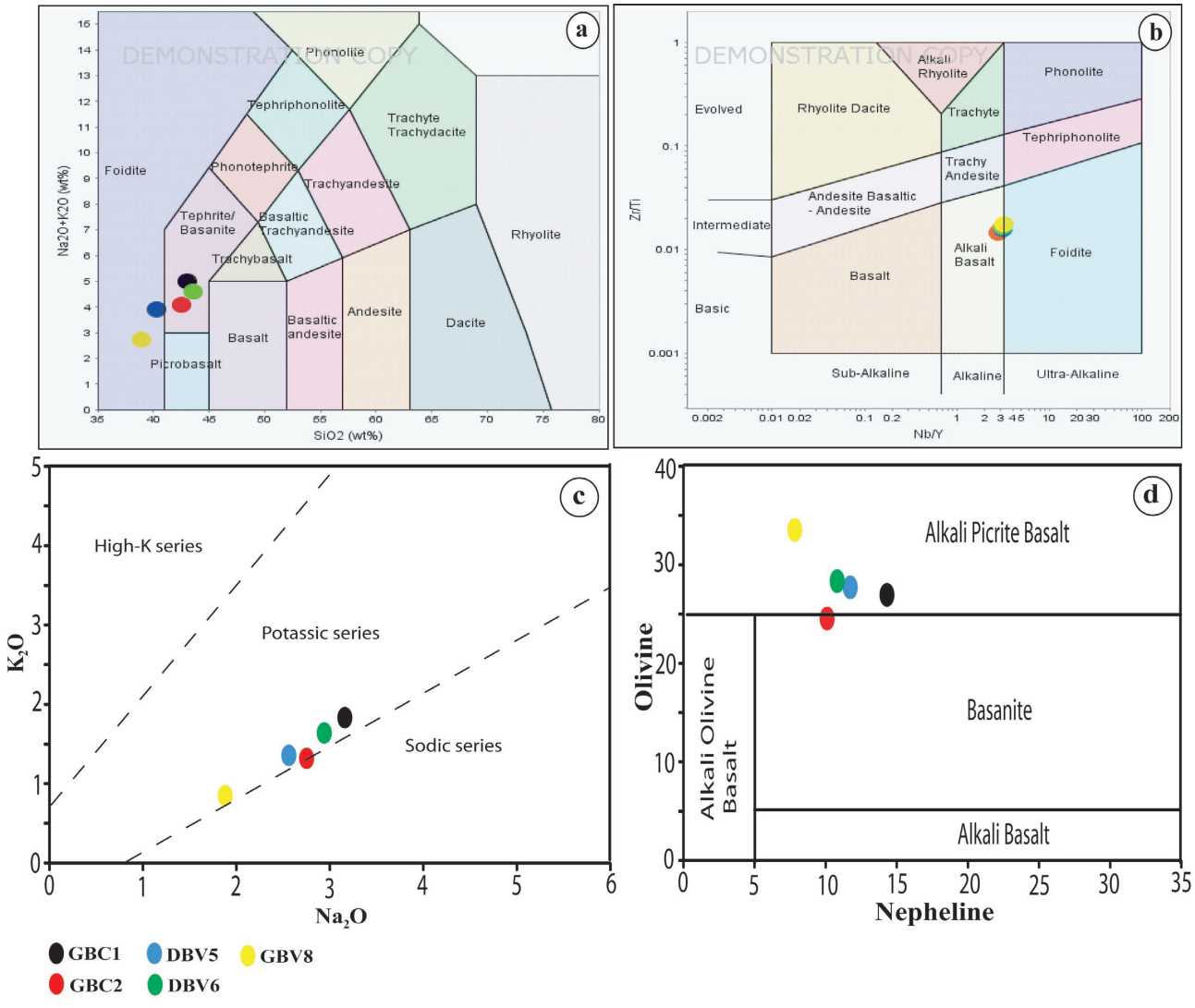

Figure 4. (a) Total Alkali vs Silica diagram (Le Bas et al., 1986) showing bulk-rock compositions for Dibi lavas. (b) Log Nb/Y vs Log Zr/Ti diagram of Dibi lavas after Pearce (1996). (c) K_2O vs. Na_2O diagram after Le Maitre (2002) shows the study samples plotting within the Potassic Series. (d) Plots of normative olivine against normative nepheline compositions of Dibi alkali lava, after Chih (1988). These same symbols will be used for all other diagrams in this work.

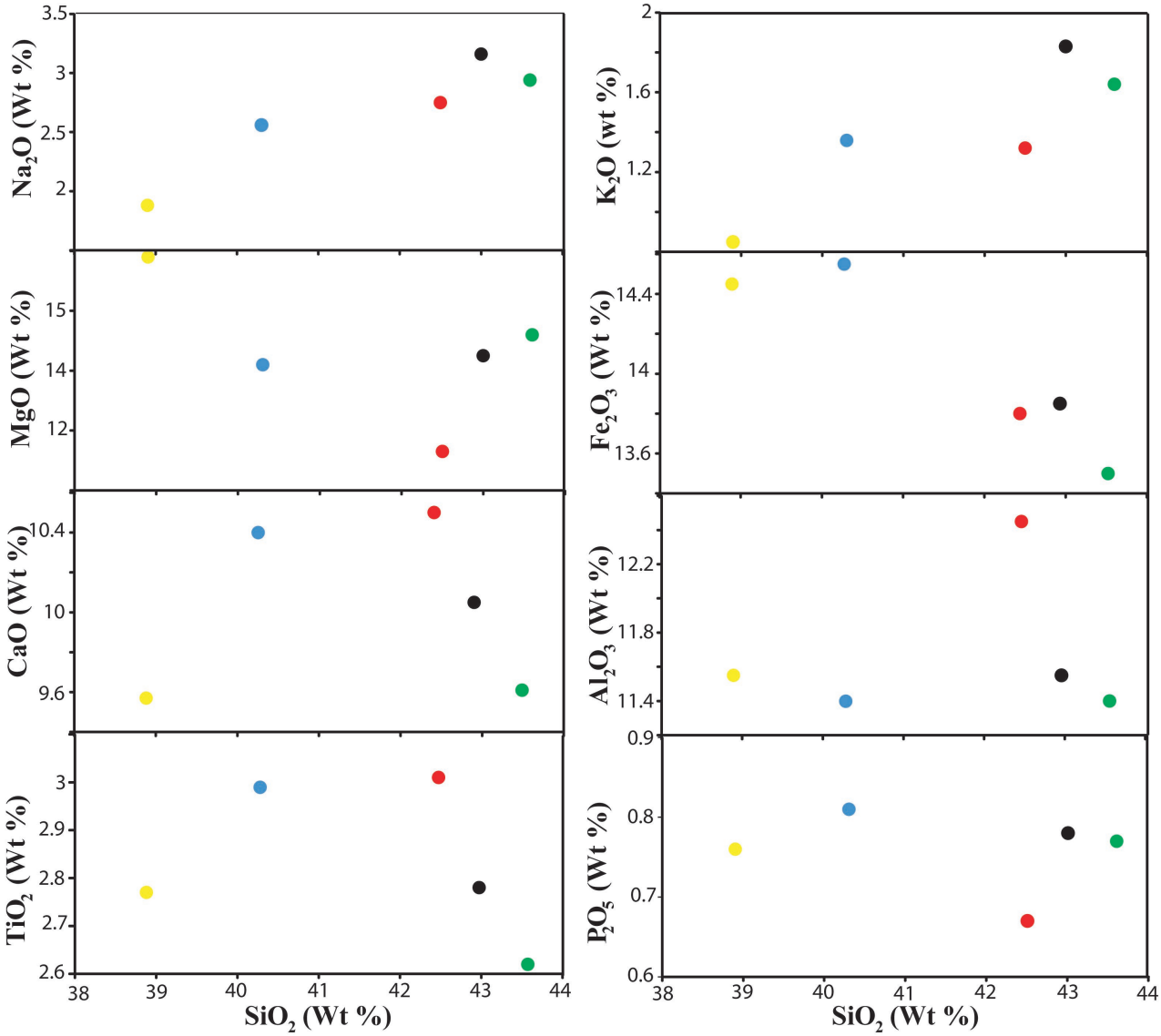

Figure 5. Major element variations for Dibi lavas plotted against their SiO_2 contents.

4.2.2. Trace Elements and REE

Primitive mantle normalized (Sun & McDonough, 1989) spider diagram of trace-element abundances for the studied lavas shows that these rocks are enriched in LILEs compared to HFSEs (**Figure 6(b)**). Most of the samples show a slightly positive Nb and Ti anomaly. The plot of REE normalized by chondrite ((Sun & McDonough, 1989) **Figure 6(a)**) shows an enrichment of LREE over HREEs for the Dibi lavas with $La/Yb_{CN} = 5.15 – 5.88$. These lavas do not show any Eu anomaly. The average value of Eu*/Eu is 0.93. All samples show similar trends, suggesting similar REE fractionation degrees and magma source. Their profiles are well correlated with Ocean Island Basalt (OIB) (**Figure 6(a)**) and are clearly distinct from Enriched Mid-Oceanic Ridge Basalt (E-MORB) and Normal Mid-Oceanic Ridge Basalt (N-MORB).

Dibi lavas have high contents of Cr (566 - 796 ppm) and V (227 - 285 ppm).

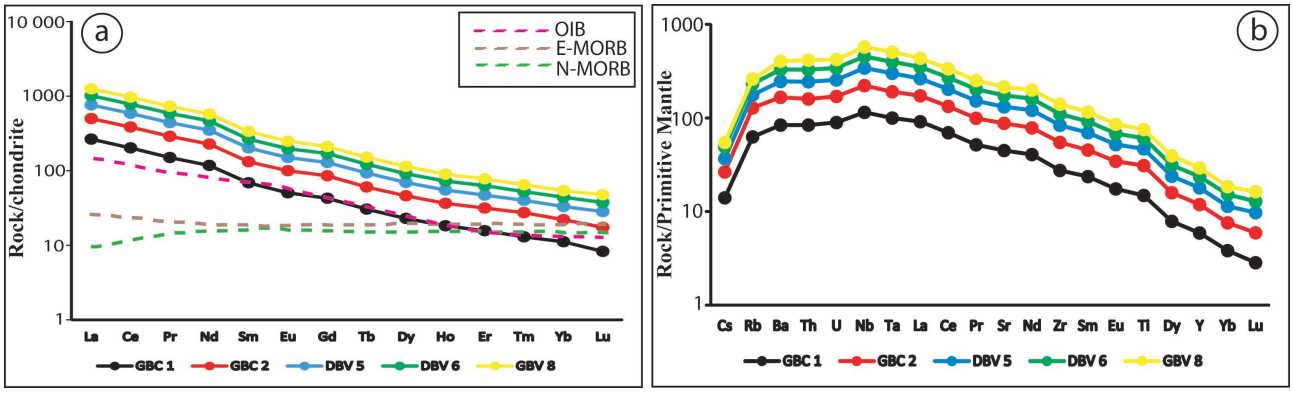

Figure 6. (a) Chondrite and (b) Primitive Mantle normalized spider diagrams of the Dibi lavas; normalization values are from Sun & McDonough (1989).

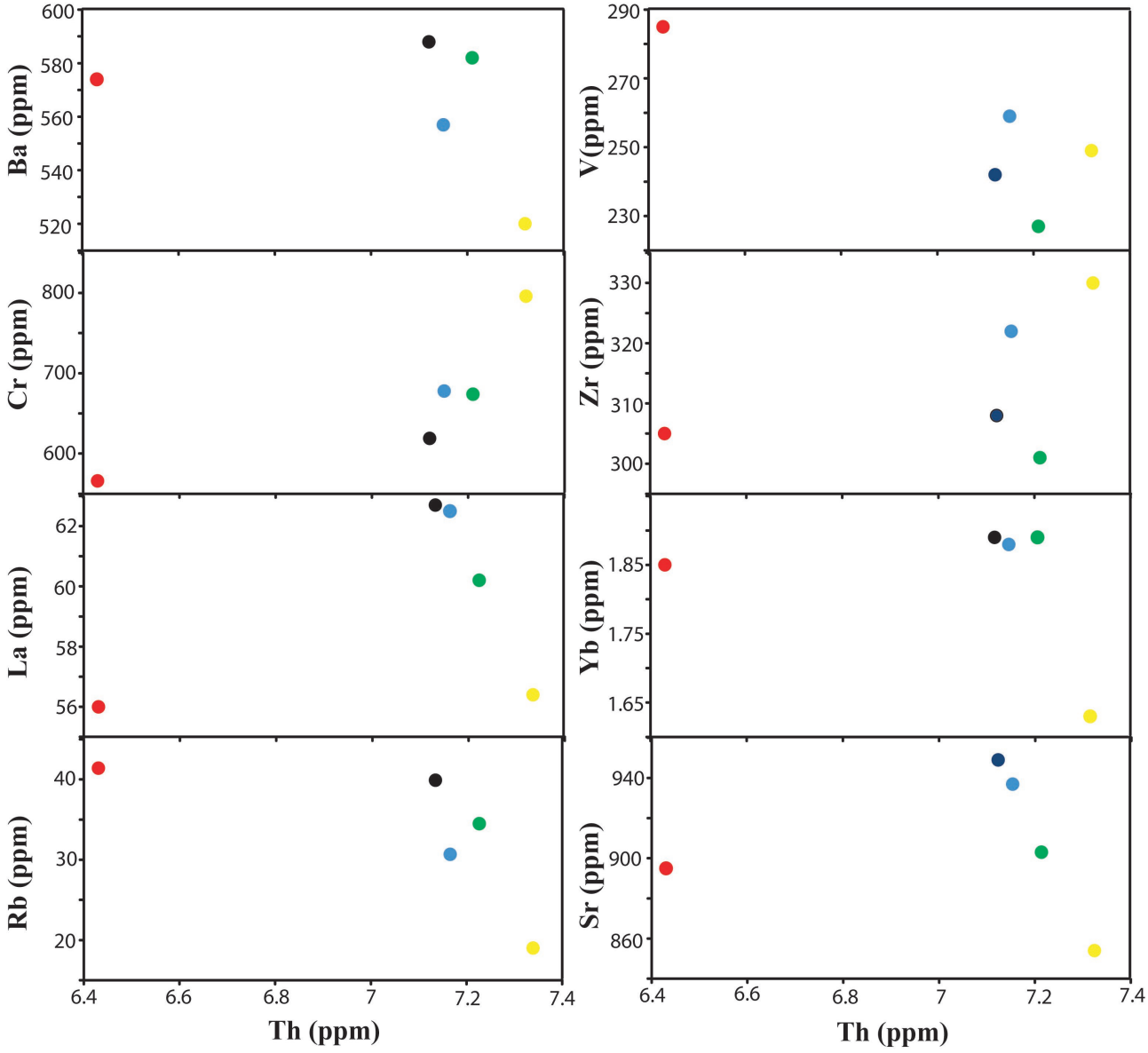

Figure 7. Trace element variations for Dibi lavas plotted against their respective Th content.

These Cr and V contents are equal to or greater than the values commonly assumed for primary magmas from peridotite (Cr: 300 - 500 ppm; V: 216 - 295 ppm (Jung & Masberg, 1998)). Thorium (6.43 - 7.32 ppm) has a mineral-liquid distribution coefficient of less than 0.01, indicating a strong preference for the melt phase (Laridhi-Ouazaa, 1989). Consequently, thorium becomes highly enriched in the residual melt during magmatic evolution. This element can serve as a differentiation index for variation diagrams (**Figure 7**). Sc (25.5 - 30.8 ppm), another compatible trace element, has low concentrations (**Table 3**). The concentrations of incompatible trace elements such as Sr (854 - 949 ppm), Ba (520 - 588 ppm), Zr (301 - 330 ppm), Nb (75.9 - 85.7 ppm), Hf (6.63 - 7.01 ppm), Ta (3.7 - 4.5 ppm), and U (1.65 - 1.88 ppm) are not very variable in these lavas.

Table 2. Whole-rock major elements data for Dibi lavas with CIPW Norm.

Rock type	Basanite	Basanite	Basanite	Nephelinite	Nephelinite
Sample	GBC1	GBC2	DBV6	DBV5	GBV8
SiO_2	43	42.5	43.6	40.3	38.9
TiO_2	2.78	3.01	2.62	2.99	2.77
Al_2O_3	11.55	12.45	11.4	11.4	11.55
Fe_2O_3	13.85	13.8	13.5	14.55	14.45
MnO	0.19	0.18	0.19	0.2	0.19
MgO	14.25	12.65	14.6	14.1	15.9
CaO	10.05	10.5	9.61	10.4	9.57
Na_2O	3.16	2.75	2.94	2.56	1.88
K_2O	1.83	1.32	1.64	1.36	0.85
P_2O_5	0.78	0.67	0.77	0.81	0.76
Cr_2O_3	0.082	0.069	0.092	0.089	0.104
BaO	0.06	0.06	0.06	0.06	0.06
LOI	-	0.65	0.42	1.05	3.06
Total	101.58	100.61	101.44	99.87	100.04
Mg#	69.8	67.3	70.8	68.5	71.2
***CIPW** Norm*					
Orthoclase	10.81	7.8	9.69	5.62	5.02
Albite	0.31	4.59	4.9	-	1.42
Anorthite	11.93	17.73	13.07	15.6	20.57
Leucite	-	-	-	1.89	-
Nepheline	14.32	10.12	10.82	11.73	7.85
Diopside	26.44	24.2	23.8	24.76	17.65
Olivine	26.93	24.52	28.31	27.71	33.52
Magnetite	2.39	2.38	2.33	2.51	2.49
Ilmenite	5.28	5.72	4.98	5.68	5.26
Apatite	1.81	1.55	1.78	1.88	1.76

Table 3. Whole-rock Trace and REE data for Dibi lavas.

Rock type	Basanite	Basanite	Basanite	Nephelinite	Nephelinite
Sample	GBC1	GBC2	DBV6	DBV5	GBV8
Ba	588	574	582	557	520
Ce	123.5	112	118.5	124.5	114.5
Cr	619	566	674	678	796
Cs	0.45	0.4	0.39	0.33	0.18
Dy	5.81	5.92	5.51	5.9	5.95
Er	2.59	2.63	2.61	2.59	2.48
Eu	2.93	2.86	2.72	2.94	2.93
Ga	20.2	20.9	19.2	19.4	19
Gd	8.79	8.78	8.45	8.9	8.38
Hf	6.63	6.92	6.71	6.89	7.01
Ho	1.03	1.04	1	1.04	0.97
La	62.7	56	60.2	62.5	56.4
Lu	0.21	0.23	0.23	0.28	0.26
Nb	81.8	75.9	79.6	85.7	85.4
Nd	55	51.2	53.6	57.5	52.2
Pr	14.3	13.15	14	14.55	13.45
Rb	39.9	41.4	34.5	30.7	19
Sc	26.1	30.8	25.5	28.5	26.3
Sm	10.5	9.66	9.72	10.8	10.8
Sn	2.4	2.7	2.3	2.8	2.8
Sr	949	895	903	937	854
Ta	4.1	3.7	4	4.5	4.4
Tb	1.14	1.12	1.08	1.22	1.12
Th	7.12	6.43	7.21	7.15	7.32
Ti	19300	21100	18100	20400	18800
Tm	0.33	0.37	0.32	0.32	0.31
U	1.88	1.68	1.82	1.8	1.65
V	242	285	227	259	249
W	1.3	0.9	1.1	1.1	1
Y	26.8	27.3	25.6	27.7	26.1
Yb	1.89	1.85	1.89	1.88	1.63
Zr	308	305	301	322	330
Eu/Eu*	0.93	0.95	0.92	0.92	0.94

4.3. Mineral Chemistry

4.3.1. Olivine

Chemical analyses of olivine crystals in the basanites and foidites are presented in **Table 4**. They are all chrysolites (**Figure 8(a)**) according to (Dick, 1989); and are magnesian, with a forsterite content varying widely in the foidites ($Fo_{77.28\text{-}87.28}$) as in the basanites ($Fo_{78.92\text{-}87.04}$). They are slightly more magnesian than olivine of Ngao Volgar ($Fo_{78.9}$ (Dili-Rake et al., 2022)) and Baossi Warack ($Fo_{76\text{-}84}$ (Tiabou et al., 2018)) in the Adamawa Plateau, but slightly less magnesian than those of Mount Cameroon (Fo_{89} (Wembenyui et al., 2020)) in the southern part of the CVL. Their Mg# varies from 77.73 to 87.85%. Olivine crystals in Dibi lavas present a wide range of compositions in both the foidites and the basanites. In the foidites, the major element contents of olivine are: MgO (38.75 - 47.20 wt.%), FeO (11.65 - 22.06 wt.%), MnO (0.12 - 0.39 wt.%), NiO (0.13 - 0.38 wt.%), and CaO (0.16 - 0.57 wt.%); in basanites they are: MgO (40.73 - 46.84 wt.%), FeO (12.42 - 19.39 wt.%), MnO (0.16 - 0.39 wt.%), NiO (0.06 - 0.35 wt.%), and CaO (0.17 - 0.42 wt.%). In all these lavas, CaO contents are high (up to 0.57 wt.%). They are different from and higher than those found in the spinel of the mantle xenoliths beneath Adamawa (Dagwai et al., 2014; Nkouandou et al., 2023) and some volcanic centers of the Cameroon Volcanic Line (Tamen et al., 2015). Such high CaO contents characterize the olivines of alkaline lavas (Roeder & Emsly, 1970). CaO and MnO contents of olivines are negatively correlated with Mg# (**Figure 8(c)-(d)**). In comparison, NiO contents are positively correlated (**Figure 8(b)**). Similar features were observed in some basalts of the CVL (Kagou et al., 2001, Nkouandou et al., 2008, Fagny et al., 2020).

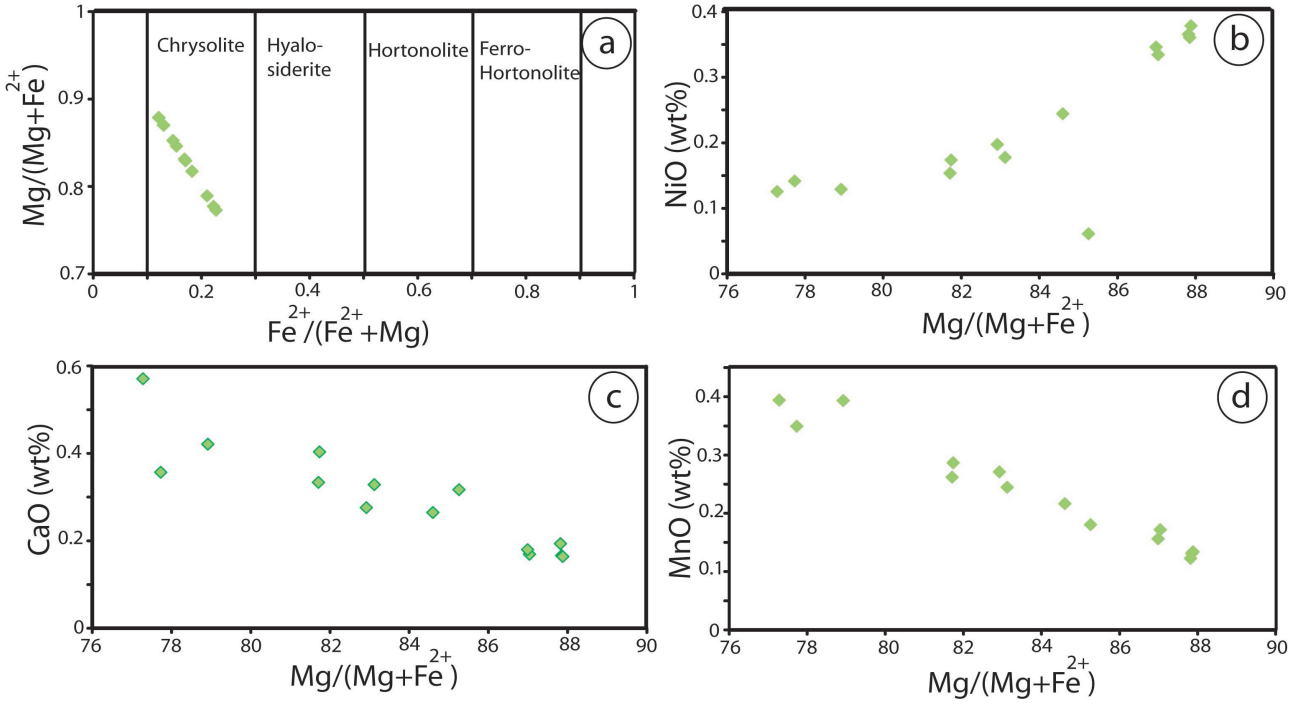

Figure 8. (a) Compositions of representative olivine crystals in Dibi lavas plotted in the [Mg/(Mg + Fe^{2+})] vs [Fe^{2+}/(Fe^{2+} + Mg)] diagram (Dick, 1989). (b), (c), (d) NiO, CaO, and MnO variations following [Mg/(Mg + Fe^{2+})] of olivine of the Dibi lavas.

4.3.2. Clinopyroxene

In the conventional Wo-En-Fs diagram (Morimoto et al., 1988), most of the clinopyroxene plots are in the diopside field and a few clinopyroxenes fall into the fassaite field (Figure 9). Clinopyroxene compositions are in the range ($Wo_{51}En_{35}Fs_{14}$) in foidites and ($Wo_{50\text{-}46.18}En_{34.8\text{-}41.29}Fs_{10.41\text{-}15.92}$) in basanites. All cpx from Dibi lavas are Ca-rich with Ca/(Ca + Mg + Fe) values ranging from 0.46 to 0.51 ($Fe = Mn + Fe^{2+} + Fe^{3+}$), with an average of 0.49 (Table 5). TiO_2 (0.23 - 4.92 wt.%), Na_2O (0.39 - 0.99 wt.%) and Al_2O_3 (2.10 - 9.43 wt.%) contents are fairly high and varied, indicating the alkali nature of these pyroxenes (Schweitzer et al., 1979). The $Fe^{2+}/(Fe^{2+} + Fe^{3+})$ values of clinopyroxenes are relatively high, ranging from 0.45 to 0.80 (with an average value of 0.65), implying that the oxygen fugacity was relatively low (Wass, 1979). The values of the Al^{VI}/Al^{IV} ratios are very low in foidites (0.003 - 0.131) and range from (0.035 - 0.863) in basanites. In basanite GBC2, one clinopyroxene crystal shows an Al^{VI}/Al^{IV} ratio of 1.067.

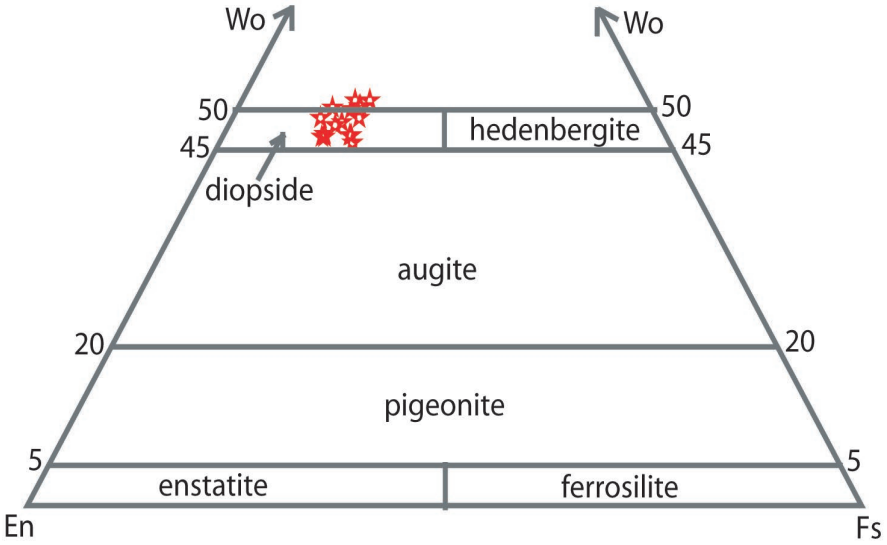

Figure 9. Wo-En-Fs classification diagram for clinopyroxenes after (Morimoto et al., 1988).

4.3.3. Feldspars

Feldspar compositions are illustrated in a ternary plot of the An-Ab-Or (Figure 10). From foidites to basanites, feldspar compositions vary from anorthoclase (solid solution of alkali feldspars) to labradorite (plagioclase). In foidites, the feldspar is typically alkaline ($Ab_{64.45\text{-}65.13}An_{6.81\text{-}9.15}Or_{26.87\text{-}27.08}$), while in basanites, the alkali type ($Ab_{60.92\text{-}64.11}An_{8\text{-}8.47}Or_{28.45\text{-}32.27}$) and plagioclase ($Ab_{37.31\text{-}39.67}An_{57.43\text{-}60.70}Or_{1.99\text{-}2.28}$) are found. Compared to plagioclases (Table 6), anorthoclases show high contents of P_2O_5 (1.24 - 2.12 wt.%) and Cl (0.22 - 0.28 wt.%), while these two elements are almost zero in plagioclases. These alkali feldspars also show higher contents of FeO (6.01 - 7.28 wt.%), MgO (1.05 - 1.26 wt.%), and TiO_2 (1.32 - 2.27 wt.%) than plagioclases: FeO (0.72 - 0.88 wt.%), MgO (0.06 - 0.09 wt.%), and TiO_2 (0.19 - 0.21 wt.%).

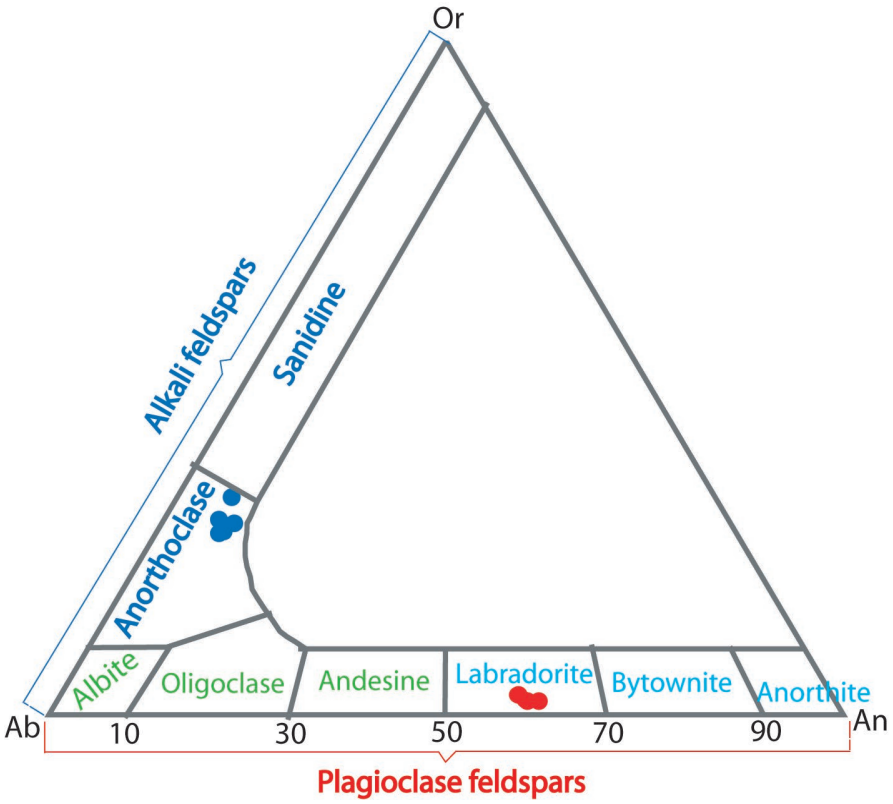

Figure 10. Feldspar crystal composition of Dibi lavas. Blue circles represent alkali feldspars, and red circles represent plagioclases.

4.3.4. Titanomagnetite

Representative chemical analyses and structural formulae of iron titanium oxides are presented in Table 7. They are present only in basanites. In the sample GBC2, the composition of titanomagnetite is characterized by TiO_2 (20.06 - 23.54 wt.%) contents higher than those of sample DBV6 (TiO_2: 15.17 - 17.06 wt.%). The contents of other oxides vary slightly between these two basanite samples: FeO (62.53 - 64.12 wt.%), MgO (4.41 - 5.61 wt.%), Al_2O_3 (3.88 - 4.58 wt.%) and Cr_2O_3 (0.26 - 1.40 wt.%) in GBC2 and FeO (63.72 - 65.74 wt.%), MgO (4.82 - 5.71 wt.%), Al_2O_3 (5.69 - 7.01 wt.%) and Cr_2O_3 (0.10 - 2.28 wt.%) in DBV6. This titanomagnetite contains up to 0.33 wt.% V_2O_3 and 0.16 wt.% ZnO.

4.3.5. Other Mineral Phases

Other mineral phases (Table 7) include spinel (Al-chromite in foidites and Ferrian chromite in basanite, see (Gawlick et al., 2015)) and apatite in the basanite GBC2. The Al-chromite oxide contents are as follows: Al_2O_3: 18.74 wt.%, Cr_2O_3: 32.69 wt.%, FeO: 29.07 wt.%, MgO: 12.49 wt.%, TiO_2: 2.79 wt.%, and CaO: 0.04 wt.%. In Ferrian chromite, these contents are Al_2O_3: 9.80 - 14.40 wt.%, Cr_2O_3: 12.78 - 23.37 wt.%, FeO: 39.94 - 53.58 wt.%, MgO: 6.81 - 11.76 wt.%, TiO_2: 5.01 - 9.27 wt.%, and CaO: 0.12 - 0.15 wt.%. Ferrian chromite is therefore more calcic and more titaniferous.

Apatite is characterized by high contents of CaO and P_2O_5, 54.62 and 42.24

wt.%, respectively. Traces of Cl (0.17 wt.%), MgO (0.27 wt.%), and FeO, with content reaching 0.46 wt.%, are present.

Table 4. Olivine analyses of Dibi lavas and structural formulae on the basis of 4 oxygen.

	DBV5							DBV6				GBC2		
SiO_2	40.54	40.43	39.30	40.13	39.34	37.33	38.57	40.03	38.82	40.07	39.34	40.37	39.60	40.43
TiO_2	0.01	0.02	0.03	0.01	0.07	0.18	0.08	0.03	0.07	0.03	0.04	0.01	0.03	0.01
Al_2O_3	0.06	0.05	0.03	0.05	0.03	0.05	0.04	0.04	0.03	0.04	0.03	0.06	0.04	0.06
Cr_2O_3	0.06	0.06	0.02	0.07	0.03	0.00	0.02	0.05	-	0.01	0.02	0.03	0.02	0.03
FeO	11.69	11.65	16.43	11.90	17.04	22.06	20.28	14.55	19.39	14.02	16.97	12.42	16.03	12.49
MnO	0.13	0.13	0.24	0.12	0.26	0.39	0.35	0.22	0.39	0.18	0.29	0.17	0.27	0.16
MgO	47.44	47.40	43.70	47.20	42.72	38.75	39.72	44.84	40.73	45.50	42.62	46.80	43.66	46.84
CaO	0.17	0.16	0.33	0.19	0.33	0.57	0.36	0.27	0.42	0.32	0.40	0.17	0.28	0.18
NiO	0.36	0.38	0.18	0.37	0.15	0.13	0.14	0.24	0.13	0.06	0.17	0.33	0.20	0.35
Total	100.47	100.29	100.26	100.03	99.97	99.45	99.55	100.26	99.99	100.22	99.88	100.35	100.12	100.53
Si (a.p.f.u)	1.001	1.000	0.992	0.996	1.001	0.977	1.001	1.004	0.999	1.000	1.002	1.001	1.001	1.001
Ti	-	-	0.001	-	0.001	0.003	0.002	0.001	0.001	0.001	0.001	-	0.001	-
Al	0.002	0.002	0.001	0.001	0.001	0.002	0.001	0.001	0.001	0.001	0.001	0.002	0.001	2
Fe^{3+}	-	-	0.013	0.005	-	0.038	-	-	-	-	-		-	
Fe^{2+}	0.242	0.241	0.334	0.242	0.362	0.444	0.440	0.305	0.417	0.293	0.361	0.258	0.339	0.259
Mn	0.003	0.003	0.005	0.003	0.006	0.009	0.008	0.005	0.009	0.004	0.006	0.004	0.006	0.003
Mg	1.747	1.748	1.645	1.746	1.620	1.511	1.537	1.677	1.562	1.693	1.618	1.730	1.645	1.729
Fo	87.54	87.57	82.00	87.27	81.11	74.87	77.04	84.10	78.12	84.74	81.04	86.69	82.37	86.64
Ca#	0.004	0.004	0.009	0.005	0.009	0.016	0.010	0.007	0.012	0.008	0.011	0.004	0.007	0.005
Mg#	87.85	87.88	83.12	87.82	81.71	77.28	77.73	84.60	78.92	85.26	81.74	87.04	82.92	86.99
Fe#	0.12	0.12	0.17	0.12	0.18	0.23	0.22	0.15	0.21	0.15	0.18	0.13	0.17	0.13

Table 5. Clipyroxene analyses of Dibi lavas and structural formulae on the basis of 6 oxygen.

	DBV 5			DBV 6					GBC 2							
SiO_2	43.01	42.87	44.12	47.70	46.26	43.96	49.07	49.41	45.90	49.38	52.38	52.09	52.20	45.35	47.33	47.18
TiO_2	4.62	4.71	4.25	2.56	3.12	4.92	1.28	1.22	3.12	1.28	0.26	0.24	0.23	3.68	2.38	3.10
Al_2O_3	8.37	9.43	8.58	5.33	7.58	8.02	5.94	5.67	7.23	5.85	2.10	2.11	2.17	7.52	6.90	5.30
Cr_2O_3	0.03	0.01	0.32	0.01	0.01	0.08	0.33	0.37	0.25	0.31	0.10	0.10	0.10	0.01	0.38	-
FeO	8.38	8.62	7.76	7.57	8.67	8.26	6.94	6.95	6.65	7.09	9.25	9.59	9.06	7.93	6.08	7.93
MnO	0.12	0.15	0.10	0.17	0.14	0.16	0.17	0.14	0.10	0.19	0.24	0.26	0.23	0.16	0.08	0.15
MgO	11.23	10.54	11.12	13.04	11.41	11.14	13.23	13.51	12.63	13.39	12.72	12.82	12.75	11.73	13.19	12.74
CaO	22.82	22.73	22.78	22.54	22.06	22.58	21.29	21.31	23.26	21.31	22.17	21.73	22.02	22.78	22.47	22.76
Na_2O	0.52	0.61	0.46	0.53	0.58	0.59	0.98	0.99	0.39	0.99	0.90	0.85	0.91	0.55	0.49	0.43
NiO	0.01	0.02	0.01	0.03	-	-	0.03	0.04	-	0.01	-	-	-	0.01	0.03	-

Continued

Total	99.12	99.67	99.49	99.47	99.84	99.72	99.26	99.61	99.51	99.79	100.13	99.78	99.67	99.73	99.33	99.58
Si (a.p.f.u)	1.628	1.616	1.663	1.783	1.734	1.656	1.823	1.828	1.714	1.824	1.948	1.945	1.949	1.700	1.763	1.768
Ti	0.131	0.133	0.121	0.072	0.088	0.139	0.036	0.034	0.088	0.036	0.007	0.007	0.006	0.104	0.067	0.087
Al	0.373	0.419	0.381	0.235	0.335	0.356	0.260	0.247	0.318	0.255	0.092	0.093	0.095	0.332	0.303	0.234
Cr	0.001	-	0.009	-	-	0.002	0.010	0.011	0.007	0.009	0.003	0.003	0.003	-	0.011	-
Fe^{3+}	0.146	0.126	0.076	0.093	0.062	0.094	0.084	0.089	0.099	0.088	0.059	0.062	0.057	0.100	0.062	0.086
Fe^{2+}	0.119	0.146	0.168	0.144	0.210	0.167	0.132	0.126	0.109	0.131	0.229	0.238	0.226	0.148	0.127	0.163
Mn	0.004	0.005	0.003	0.005	0.004	0.005	0.005	0.004	0.003	0.006	0.008	0.008	0.007	0.005	0.003	0.005
Mg	0.634	0.592	0.625	0.727	0.638	0.626	0.733	0.745	0.703	0.737	0.706	0.714	0.710	0.655	0.732	0.712
Ca	0.925	0.918	0.920	0.903	0.886	0.912	0.847	0.845	0.931	0.844	0.884	0.869	0.881	0.915	0.897	0.914
Na	0.039	0.044	0.034	0.038	0.042	0.043	0.071	0.071	0.028	0.071	0.065	0.062	0.066	0.040	0.035	0.031
Wo	50.730	51.523	51.412	48.383	49.341	50.705	47.189	46.798	50.548	46.872	47.083	46.178	47.024	50.299	49.313	48.767
En	34.735	33.229	34.918	38.933	35.515	34.817	40.801	41.285	38.179	40.964	37.591	37.907	37.877	36.037	40.278	37.971
Fs	14.535	15.248	13.671	12.683	15.144	14.478	12.010	11.917	11.272	12.164	15.327	15.915	15.099	13.664	10.409	13.261
Al^{VI}	0.001	0.035	0.044	0.018	0.070	0.012	0.083	0.075	0.032	0.079	0.040	0.038	0.044	0.032	0.066	0.002
Al^{IV}	0.372	0.384	0.337	0.217	0.266	0.344	0.177	0.172	0.286	0.176	0.052	0.055	0.051	0.030	0.237	0.232
Al^{VI}/Al^{IV}	0.003	0.091	0.131	0.083	0.263	0.035	0.469	0.436	0.112	0.449	0.769	0.691	0.863	1.067	0.278	0.009
Fe#	0.45	0.54	0.69	0.61	0.77	0.64	0.61	0.59	0.52	0.60	0.80	0.79	0.80	0.60	0.67	0.66
Ca#	0.51	0.51	0.51	0.48	0.49	0.51	0.47	0.47	0.50	0.47	0.47	0.46	0.47	0.50	0.49	0.49

Table 6. Feldspar analyses of Dibi lavas and structural formulae on the basis of 8 oxygen.

	DBV5			DBV6				GBC2		
SiO_2	49.37	49.92	52.62	50.95	50.99	53.06	52.99	52.12	52.70	52.68
TiO_2	1.32	1.35	1.57	1.89	2.27	0.20	0.20	0.21	0.19	0.19
Al_2O_3	20.67	20.46	20.16	20.31	20.36	27.91	28.05	28.65	28.24	28.51
FeO	7.28	6.95	6.37	6.07	6.01	0.81	0.88	0.81	0.72	0.75
MgO	1.14	1.09	1.26	1.05	1.08	0.09	0.09	0.06	0.07	0.08
CaO	2.15	1.99	1.54	2.32	1.74	11.74	11.80	12.60	12.03	12.23
Na_2O	9.05	8.97	7.63	8.75	8.93	4.48	4.46	4.28	4.42	4.41
K_2O	5.78	5.63	6.14	6.06	6.14	0.50	0.51	0.35	0.39	0.35
Cl	0.25	0.27	0.22	0.24	0.28	-	0.01	-	-	-
P_2O_5	2.12	1.94	1.24	1.92	1.58	0.05	0.05	0.04	0.05	0.03
Total	99.15	98.57	98.74	99.58	99.39	98.84	99.03	99.11	98.81	99.24
Si (a.p.f.u)	2.249	2.286	2.413	2.313	2.310	2.438	2.431	2.390	2.422	2.411
Ti	0.045	0.046	0.054	0.065	0.077	0.007	0.007	0.007	0.007	0.006
Al	1.110	1.104	1.090	1.087	1.087	1.512	1.516	1.548	1.530	1.537
Fe^{3+}	0.277	0.266	0.244	0.230	0.228	0.013	0.034	0.031	0.028	0.029

Continued

Fe^{2+}	-	-	-	-	-	0.018	-	-	-	-
Mg	0.078	0.074	0.086	0.071	0.073	0.006	0.006	0.004	0.005	0.005
Ca	0.105	0.098	0.076	0.113	0.084	0.578	0.580	0.619	0.592	0.600
Na	0.800	0.797	0.678	0.770	0.785	0.399	0.396	0.381	0.393	0.392
K	0.336	0.329	0.359	0.351	0.355	0.029	0.030	0.020	0.023	0.020
An	8.473	7.997	6.808	9.151	6.880	57.430	57.636	60.695	58.719	59.290
Ab	64.451	65.132	60.924	62.402	64.111	39.669	39.377	37.314	39.003	38.707
Or	27.077	26.872	32.268	28.447	29.009	2.901	2.987	1.990	2.278	2.003

Table 7. Titanomagnetite, chromite and apatite analyses of Dibi lavas.

–	Titano magnetite								Chomite			Apatite
	DBV5			DBV6			GBC2		DBV5	DBV6		GBC2
SiO_2	0.12	0.15	0.14	0.12	0.16	0.09	0.12	0.10	0.15	0.83	0.11	0.15
TiO_2	16.51	17.06	15.17	16.12	16.98	23.54	20.25	20.06	2.79	5.01	9.27	-
$Al2O_3$	7.01	6.92	6.42	5.97	5.69	3.88	4.42	4.58	18.74	14.39	9.80	-
Cr_2O_3	1.83	0.54	2.28	1.27	0.10	0.26	2.20	1.40	32.69	23.37	12.78	-
FeO	63.59	64.45	63.72	64.60	65.74	62.53	63.71	64.12	29.07	39.94	53.58	0.46
MnO	0.47	0.54	0.53	0.52	0.61	0.70	0.70	0.70	0.19	0.28	0.43	0.02
MgO	5.29	4.82	5.63	5.71	4.82	5.61	4.38	4.41	12.49	11.76	6.81	0.27
CaO	0.24	0.14	0.19	0.21	0.23	0.07	0.08	0.11	0.04	0.12	0.15	54.62
Na_2O	-	-	-	-	-	-	-	-	-	-	-	0.03
K_2O	-	-	-	-	-	-	-	-	-	-	-	0.00
NiO	0.07	0.05	0.14	0.08	0.04	0.06	0.05	0.05	0.23	0.15	0.09	0.01
ZnO	0.12	0.08	0.10	0.11	0.09	0.08	0.14	0.16	0.14	0.10	0.15	-
V_2O_3	0.24	0.31	0.22	0.24	0.27	0.33	0.31	0.32	0.10	0.11	0.15	-
Cl	-	-	-	-	-	-	-	-	-	-	-	0.17
P_2O_5	-	-	-	-	-	-	-	-	-	-	-	42.24
Total	95.49	95.06	94.54	94.94	94.73	97.15	96.37	96.01	96.63	96.06	93.32	97.97

5. Discussion

5.1. Tectonic Setting and Origin of Magmas

In the TiO_2-Na_2O-MnO discrimination diagram of clinopyroxenes (**Figure 11(a)**; (Nisbet & Pearce, 1977)), the majority of clinopyroxenes are concentrated in the WPA field, suggesting that the studied lavas are within-plate basalts. This is consistent with the geotectonic scenario of magmatic evolution along the CVL, which implies a pulse of anorogenic alkaline magmatism with an intraplate character favored by major faults that cut the Pan-African crystalline rocks of the Central African Fold Belt (Njonfang et al., 2013).

In the Zr/Y vs. Nb/Y and Nb/Th vs. Zr/Nb (**Figure 11(b)-(c)**) diagrams, the Dibi lavas are compared to those of Wakwa (Onana François Xavier et al., 2022), in the same region (Adamawa), and to those of Bana (Kuepouo et al., 2006), a little further south. The Dibi lavas overlap those studied at Wakwa. They are similar to magmas with an Oceanic Island Basalt (OIB) signature, showing affinity to High-μ (HIMU), Enriched type I (EM1), and recycled components, representing the basalts generated by a mantle plume (Tsafack et al., 2009). All the samples display a uniform pattern on the chondrite-normalized REE (**Figure 6(a)**) resembling that of typical OIB or intraplate alkaline igneous rocks. This indicates that all samples have the same enriched magmatic source.

These findings indicate that the Dibi lavas formed within an intraplate tectonic setting. Keller & Schoene (2018) note that intraplate continental basaltic rocks are predominantly generated through the partial melting of the asthenospheric mantle beneath a substantial continental lithosphere. This interpretation aligns with geophysical research conducted in the Adamawa region (Poudjom Djomani et al., 1995), which also highlights lithospheric thinning and identifies the Moho at approximately twenty kilometers in depth.

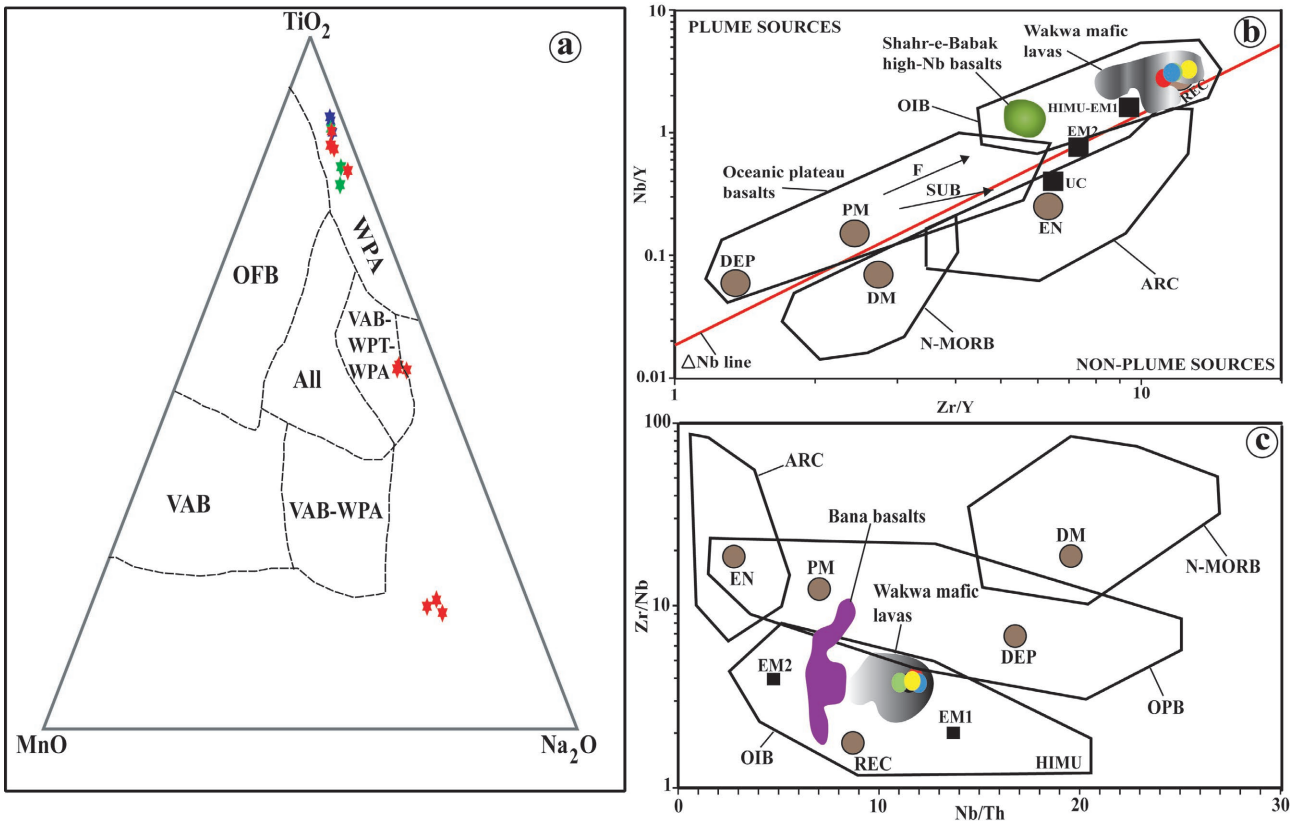

Figure 11. (a) composition of pyroxene of Dibi lavas in the TiO_2-MnO-Na_2O tectonic discrimination diagram after (Nisbet & Pearce, 1977). WPA: within-plate alkali basalt, OFB: ocean floor basalt, WPT: within-plate tholeiitic basalt, and VAB: volcanic arc basalt. (b) studied lavas in the Zr/Y vs. Nb/Y diagram, relative to the mantle compositional components (circles) and fields of rocks from different tectonic settings after (Condie, 2005). (c) Nb/Th vs. Zr/Nb diagram after (Weaver, 1991). DM: Depleted Mantle, PM: Primitive Mantle, DEP: Deep Depleted Mantle, ARC: Arc-related basalts, OPB: Oceanic Plateau Basalt, UC: upper crust, REC: Recycled Component, EN: Enriched component, EM1 and EM2: Enriched Mantle sources, HIMU: high U/Pb mantle source.

A central issue in the study of basaltic magma is determining whether its origin is lithospheric or asthenospheric. Trace element analysis plays a pivotal role in elucidating the source and characteristics of basaltic magmas. For instance, the HFSE/LREE ratio can indicate the parental magma's source: ratios less than one typically suggest derivation from the lithospheric mantle, while ratios exceeding one are indicative of an asthenospheric mantle origin (Smith et al., 1999; Ali et al., 2013). The Dibi lavas exhibit Nb/La (1.30 - 1.51), Zr/La (4.91 - 5.85), and Zr/Ce (2.49 - 2.88) values consistent with an OIB-like asthenospheric mantle source. The elemental ratios (Zr/Nb = 3.76 - 4.02, La/Nb = 0.66 - 0.77, and Ba/Th = 71. 04 - 89.27) further support a HIMU-OIB signature for these lavas (Weaver, 1991). Additionally, the notably low (Rb, U)/Nb ratios (0.22 - 0.55 and 0.019 - 0.023, respectively) align with geochemical characteristics typical of rocks displaying HIMU-OIB signatures (Kawabata et al., 2011).

5.2. Crustal Contamination

As magma ascends to the surface, its interaction with surrounding rocks frequently alters its composition. Notably, as illustrated in **Figure 2**, in addition to mantle xenoliths, the examined alkaline lavas commonly contain crustal xenoliths. Isotopic analyses typically provide clear evidence of contamination by these crustal materials. However, when such analyses are unavailable, the effects of the traversed rocks can often be inferred from variations in certain trace element concentrations and ratios (Ali et al., 2013; Dili-Rake et al., 2022). Accordingly, the discussion of Dibi lava contamination herein is based on its geochemical characteristics.

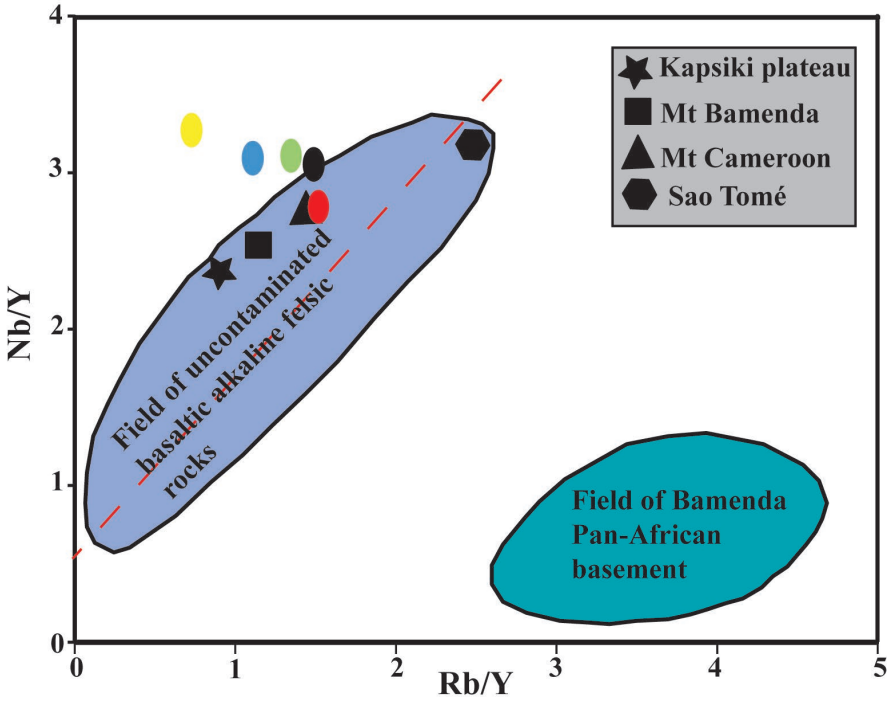

Figure 12. Dibi lavas in the Rb/Y vs. Nb/Y diagram after Cox & Hawkesworth (1985).

Referring to studies conducted by Hart et al. (1989), basaltic magmas affected by crustal contamination exhibit La/Nb ratios > 1.5 and La/Ta > 22. Furthermore, Cai et al. (2010) show that, very often, crustally contaminated mafic rocks show negative Nb and Zr and positive Sr anomalies on the multi-element diagram.

The studied lavas do not show any of these geochemical features (**Figure 6**), with La/Nb (0.66 - 0.77) and La/Ta (12.82 - 15.29) ratios. In the Rb/Y vs Nb/Y diagram of Cox & Hawkesworth (1985), **Figure 12**, only the basanites GBC2 and GBC1 are positioned within the field of uncontaminated alkali basalts and felsic rocks. The other basanite (DBV6) is not found there (this could be due to metasomatic effects) but is very close to it, as are the foidites, which remain close to the field of uncontaminated alkali basalts and felsic rocks but very far from the Pan-African basement field of Bamenda defined by (Kamgang et al., 2010). All these observations show that the magmas underwent little or no crustal contamination; the presence of mantle xenoliths in many of these lavas indicates that the ascent of the alkaline magma was rapid enough to minimize contamination.

5.3. Mantle Source and Degree of Partial Melting

Basalts have long been considered to be the result of the partial melting of peridotite. However, numerous experimental studies have demonstrated that silica-deficient alkali basalts can also originate from the melting of other mantle lithologies such as silica-poor eclogite and garnet pyroxenite, hornblendite, and carbonated peridotite (Dasgupta et al., 2010; Yuan et al., 2020).

Recently, some researchers (Herzberg & Asimow, 2008; Yang & Zhou, 2013; Yuan et al., 2020) have successfully used the MgO, CaO, and Yb contents, Fe/Mn and Dy/Yb ratios, and the FC3MS parameter ($FeOt/CaO-3\times MgO/SiO_2$) to determine the nature of the source lithology of lavas.

To identify the mantle source lithology of Dibi lavas, we used the MgO versus CaO diagram (whole-rock data) from Herzberg & Asimow (2008) (**Figure 13**). This diagram indicates that the source lithology of Dibi lavas is peridotite.

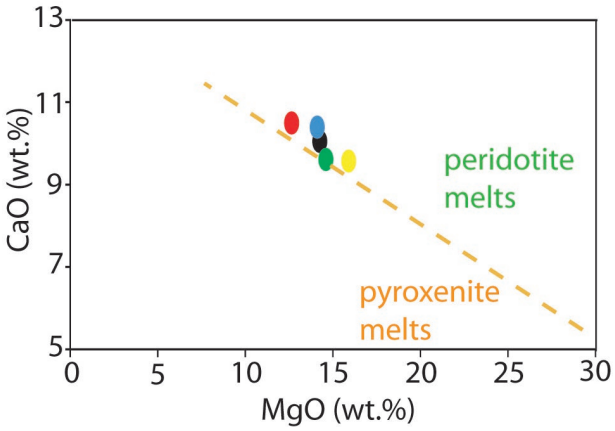

Figure 13. A plot of MgO (wt.%) versus CaO (wt.%) highlights the experimental distinc tion between melts derived from peridotite and those from pyroxenite sources (Herzberg and Asimow, 2008).

The relative depletions in HREE and Y presented by the Dibi samples (**Figure 6**) suggest the presence of garnet in the mantle source. This is because garnet can retain HREE during partial melting (Goldstein & Francis, 2008; Dili-Rake, 2022). The studied lavas also present ratios of Y/Yb = 13.54 - 16.01 (> 10) and (Ho/Yb)N = 1.59 - 1.79 (> 1.2), indicative of garnet as a residual phase in the mantle source during the partial melting processes (Ge et al., 2002).

Using the Gd/Yb versus La/Yb diagram from Yokoyama et al. (2007), the high Gd/Yb ratio indicates more than 8% garnet in the source. Similar garnet content was reported in the source of Baossi-Warack (Adamawa plateau (Tiabou et al., 2018)) and the Debunscha maar (south of the CVL at the ocean-continent boundary (Ngwa et al., 2017)). Such a large amount of garnet in the source suggests that melting took place within the garnet-stable depth (≥ 80 km (Niu, 2005)).

The high Ce_N/Y_N ratios (10.52 - 11.87) suggest a lower degree of partial melting in the generation of Dibi lavas than for Ascension and Bouvet, other OIBs (with Ce_N/Y_N ratios of 4.6 and 3.9, respectively, (Weaver et al., 1987)). This partial melting rate is about 3% - 5% (**Figure 14**).

These degrees of partial melting are higher than the ones inferred at Baossi-Warack (0.5% - 2%) (Tiabou et al., 2018) and Mt. Cameroon (1% - 3%) (Yokoyama et al., 2007) but lower than those of Barombi Koto Volcanic Field (8% - 10%) (Tamen et al., 2007) and Mounts Bangou and Bana (15% - 16%) (Fosso et al., 2005; Kuepouo et al., 2006). Dibi's 3% - 5% partial melting reflects an intermediate mantle process, shallower and more extensive than that of Baossi-Warack and Mt. Cameroon, but not as intense or voluminous as the melting observed at Bangou or Barombi Koto. It suggests a **moderate mantle temperature or decompression** event, possibly contributing to **moderate volcanic activity** in terms of volume and explosivity.

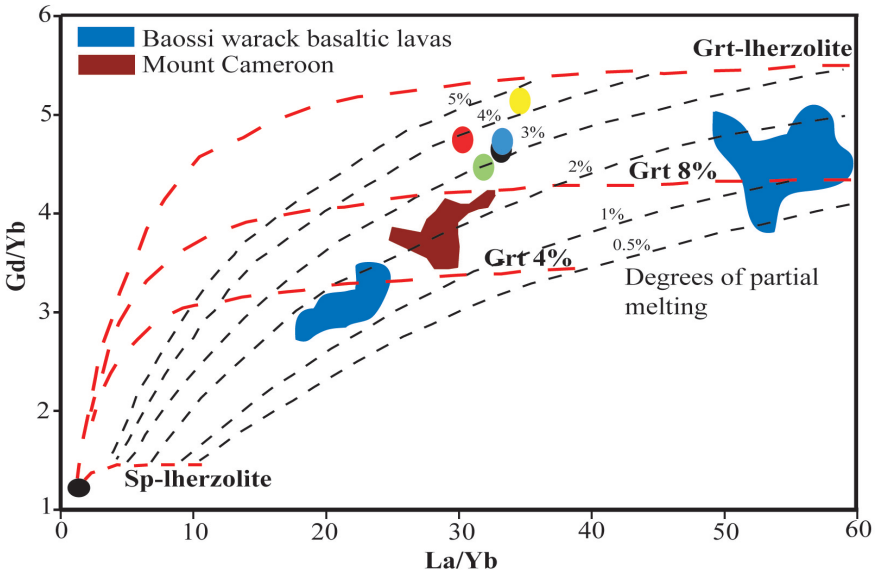

Figure 14. La/Yb vs. Gd/Yb diagram after (Yokoyama et al., 2007), showing degrees of partial melting for Dibi lavas. Curves with Grt 4% and Grt 8% after (Halliday et al., 1995) represent the garnet contents of the source.

5.4. Evidence of Fractional Crystallization in Dibi lavas

Primary magmas in equilibrium with mantle peridotites typically exhibit high Mg numbers (Mg# = 68 - 72) and elevated chromium contents (approximately 1000 ppm) (Tatsumi et al., 1983). The Dibi lavas display Mg# values ranging from 67.3 to 71.2, consistent with derivation from primary mantle-derived melts. However, their Cr concentrations (566 - 796 ppm) are notably lower than expected for primitive melts, suggesting that fractional crystallization has modified the original composition. Geochemical trends observed in major element data support this interpretation. In the Dibi lavas, negative correlations between SiO_2 and MgO, Fe_2O_3-TiO_2, CaO, and P_2O_5 (**Figure 5**) indicate the fractional removal of olivine, Fe-Ti oxides, clinopyroxene, plagioclase, and apatite. These trends are consistent with mineral fractionation processes typical of alkaline magmatic systems. Additional petrographic and geochemical features reinforce the role of fractional crystallization in the evolution of the Dibi magmas. These include:

- The presence of opaque oxide inclusions within olivine, and olivine inclusions within clinopyroxene.
- Resorbed olivine crystals (**Figure 3(d)**) and corroded crystal margins are indicative of disequilibrium during crystallization, likely due to changes in melt composition.
- Parallel rare earth element (REE) patterns, which imply coherent magmatic evolution (De Souza et al., 2007) (**Figure 6**), are observed.
- Depletion of compatible trace elements (e.g., Cr, Sc, V), which are preferentially incorporated into early-crystallizing ferromagnesian minerals (Wilson, 1992).

Together, these petrographic and geochemical observations indicate that the Dibi alkaline lavas evolved through fractional crystallization of olivine, clinopyroxene, plagioclase, Fe-Ti oxides, and apatite, as is the case for the entire CVL (Fitton, 1987; Yokoyama et al., 2007; Kamgang et al., 2013; Tiabou et al., 2018).

5.5. Clinopyroxene-Based Geothermobarometry

The partitioning of aluminum between the tetrahedral (Al^{IV}) and octahedral (Al^{VI}) sites in clinopyroxene is closely linked to the physicochemical conditions under which the mineral crystallized. As originally proposed by Thompson (1947) and Poldervaart & Hess (1951), aluminum preferentially occupies the tetrahedral site at higher temperatures, while it tends to enter the octahedral site under higher pressure conditions.

In the Al^{IV} vs. Al^{VI} diagram (**Figure 15**), clinopyroxenes from the Dibi alkaline lavas predominantly plot within the igneous field (low pressure) defined by Aoki & Kushiro (1968) and later refined by Aoki & Shiba (1973). Notably, most clinopyroxene crystals from the basanite sample GBC2 plot in the intermediate field, corresponding to the granulite domain, indicating crystallization conditions distinct from those typical of both eclogitic and primary igneous environments.

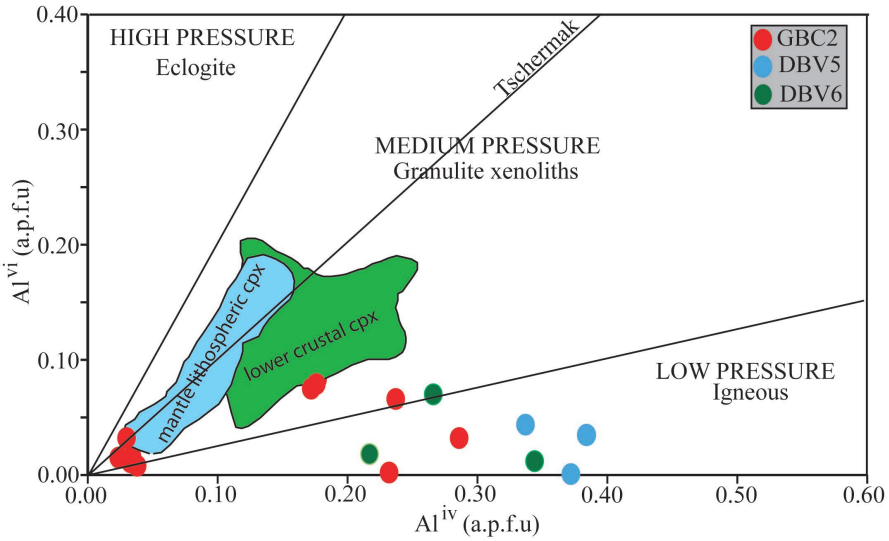

Figure 15. Plot of Dibi lavas clinopyroxene in the Al^{IV} vs. Al^{VI} diagram of Aoki & Kushiro (1968). The lower crust and mantle lithospheric Cpx domains are from Jankovics et al. (2013).

These observations suggest that clinopyroxenes from the Dibi lavas crystallized under medium to low-pressure conditions, consistent with rapid magma ascent. The lack of prolonged residence in deep-seated magma chambers allowed crystallization to occur during decompression and cooling at relatively shallow crustal levels, likely during the final stages of magma ascent. This interpretation is further supported by the V_{cell} vs. V_{M1} diagram of Nimis (1999), which indicates crystallization pressures below 10 kbar (**Figure 16**). Such pressures are typical of basaltic systems associated with mid-ocean ridges, ocean-island hotspots, or continental

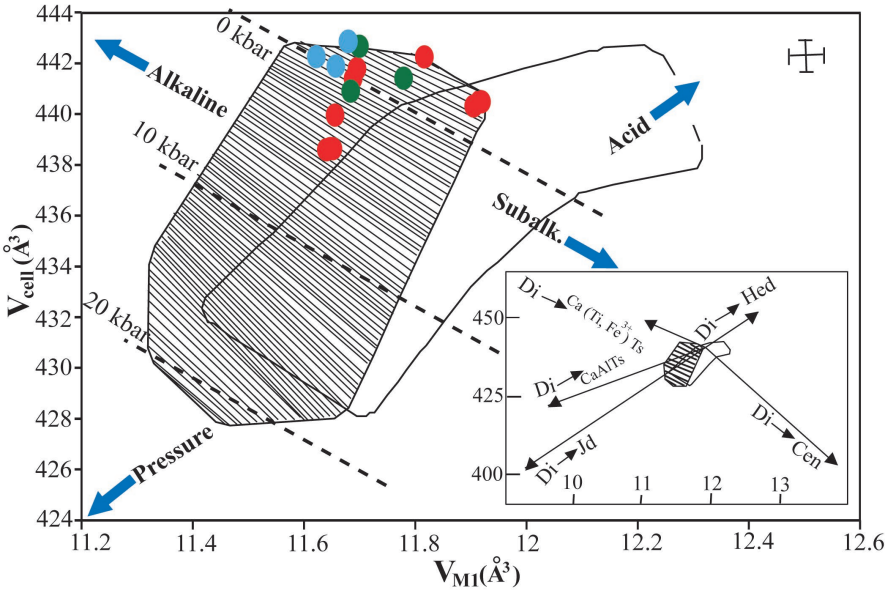

Figure 16. Position of clinopyroxenes from Dibi Lavas in the Vcell vs. V_{M1} diagram of Nimis (1999), with isobars (dashed lines) for basic and ultrabasic anhydrous systems (Nimis & Ulmer, 1998). Vcell and V_{M1} were calculated following Nimis (1999).

rift settings. Additionally, using the clinopyroxene-liquid geothermobarometer of Neave & Putirka (2017), equilibrium conditions for the studied clinopyroxenes suggest crystallization temperatures between 981.6˚C and 1051.6˚C, and pressures ranging from 0.9 to 1.6 kbar.

These results collectively support a model of shallow-level crystallization, characteristic of rapidly ascending magmas in intraplate volcanic settings such as the Cameroon Volcanic Line.

6. Conclusion

Dibi village contains Strombolian cones and maars; basalts from these two systems often contain crustal and mantle xenoliths. This study focuses on petrographic, whole-rock geochemical, and mineralogical analyses of Dibi lavas with the aim of identifying magmatic processes and determining the tectonic setting and the nature of the source of magmatism in this part of the Adamawa Volcanic field. These lavas from Dibi village are basanites and foidites with a porphyritic microlithic texture. They contain olivine, clinopyroxene, plagioclase, and alkali feldspars as the main mineral phases, accompanied by Fe-Ti oxides, chromites, and apatite. The compositions of major, trace, and RE elements show that these lavas are within-plate basalts and are similar to magmas with an Oceanic Island Basalt (OIB) signature with affinity to High-μ (HIMU), Enriched type I (EM1), and recycled component, characteristics of basalts generated by a mantle plume. They also show that these lavas are uncontaminated and were produced by a low degree of partial melting (3%- 5%) of a garnet peridotite asthenosphere source.

Acknowledgements

The authors are thankful to the Department of Lithospheric Research of the University of Vienna (Austria) for the EMPA.

Conflicts of Interest

The authors declare no conflicts of interest regarding the publication of this paper.

References

Ali, S., Ntaflos, T., & Upton, B. G. J. (2013). Petrogenesis and Mantle Source Characteristics of Quaternary Alkaline Mafic Lavas in the Western Carpathian-Pannonian Region, Styria, Austria. *Chemical Geology, 337,* 99-113. https://doi.org/10.1016/j.chemgeo.2012.12.001

Aoki, K. I., & Kushiro, I. (1968). Some Clinopyroxenes from Ultramafic Inclusions in Dreiser Weiher, Eifel. *Contributions to Mineralogy and Petrology, 18,* 326-337. https://doi.org/10.1007/bf00399694

Aoki, K., & Shiba, I. (1973). Pyroxenes from Lherzolite Inclusions of Itinome-Gata, Japan. *Lithos, 6,* 41-51. https://doi.org/10.1016/0024-4937(73)90078-9

Asaah, A. N. E., Yokoyama, T., Aka, F. T., Usui, T., Wirmvem, M. J., Tchamabe, B. C. et al. (2014). A Comparative Review of Petrogenetic Processes beneath the Cameroon Volcanic Line: Geochemical Constraints. *Geoscience Frontiers, 6,* 557-570. https://doi.org/10.1016/j.gsf.2014.04.012

Cai, K., Sun, M., Yuan, C., Zhao, G., Xiao, W., Long, X. et al. (2010). Geochronological and Geochemical Study of Mafic Dykes from the Northwest Chinese Altai: Implications for Petrogenesis and Tectonic Evolution. *Gondwana Research, 18,* 638-652. https://doi.org/10.1016/j.gr.2010.02.010

Chih, C. S. (1988). *The Study of Cenozoic Basalts and the Upper Mantle Beneath Eastern China (Attachment: Kimberlites)* (p. 277). China Geosciences University Press.

Condie, K. C. (2005). High Field Strength Element Ratios in Archean Basalts: A Window to Evolving Sources of Mantle Plumes? *Lithos, 79,* 491-504. https://doi.org/10.1016/j.lithos.2004.09.014

Cox, K. G., & Hawkesworth, C. J. (1985). Geochemical Stratigraphy of the Deccan Traps at Mahabaleshwar, Western Ghats, India, with Implications for Open System Magmatic Processes. *Journal of Petrology, 26,* 355-377. https://doi.org/10.1093/petrology/26.2.355

Dagwai, N., Gilles, C., Pierre, K., Bertrand, M. G. I., & Ismaïla, N. (2014). Spinel-Bearing Lherzolite Xenoliths from Hosséré Garba (Likok, Adamawa-Cameroon): Mineral Compositions and Geothermobarometric Implications. *International Journal of Geosciences, 5,* 1435-1444. https://doi.org/10.4236/ijg.2014.512117

Dasgupta, R., Jackson, M. G., & Lee, C. A. (2010). Major Element Chemistry of Ocean Island Basalts—Conditions of Mantle Melting and Heterogeneity of Mantle Source. *Earth and Planetary Science Letters, 289,* 377-392. https://doi.org/10.1016/j.epsl.2009.11.027

De Souza, Z. S., Martin, H., Peucat, J., Jardim De Sá, E. F., & Macedo, M. H. D. F. (2007). Calc-alkaline Magmatism at the Archean-Proterozoic Transition: The Caicó Complex Basement (NE Brazil). *Journal of Petrology, 48,* 2149-2185. https://doi.org/10.1093/petrology/egm055

Déruelle, B., Moreau, C., Nkoumbou, C., Kambou, R., Lissom, J., Njonfang, E. et al. (1991). The Cameroon Line: A Review. In A. B. Kampunzu, & R. T. Lubala (Eds.), *Magmatism in Extensional Structural Settings* (pp. 274-327). Springer. https://doi.org/10.1007/978-3-642-73966-8_12

Dick, H. J. B. (1989). Abyssal Peridotites, Very Slow Spreading Ridges and Ocean Ridge Magmatism. *Geological Society, London, Special Publications, 42,* 71-105. https://doi.org/10.1144/gsl.sp.1989.042.01.06

Dili-Rake, J., Abdoulaye, S. A., Tchop, J. L., Teitchou, M. I., Bouba, C. M., Nkouandou, O. F. et al. (2022). Magmatism of the Beka Volcanic Massifs (Cameroon Volcanic Line, West-Central Africa): New Petrographical and Mineralogical Data. *Journal of Geoscience and Environment Protection, 10,* 198-228. https://doi.org/10.4236/gep.2022.107013

Dorbath, C., Dorbath, L., Fairhead, J. D., & Stuart, G. W. (1986). A Teleseismic Delay Time Study across the Central African Shear Zone in the Adamawa Region of Cameroon, West Africa. *Geophysical Journal International, 86,* 751-766. https://doi.org/10.1111/j.1365-246x.1986.tb00658.x

Dumont, J. F. (1987). Étude structurale des bordures nord et sud du plateau de l'Adamaoua: Influence du contexte atlantique. *Géodynamique, 2,* 55-68.

Fagny, A. M., Nkouandou, O. F., Bardintzeff, J. M., Guillou, H., Iancu, G. O., Ndassa, Z. N. N. et al. (2020). Petrology and Geochemistry of the Tchabal Mbabo Volcano in Cameroon Volcanic Line (Cameroon, Central Africa): An Intra-Continental Alkaline Volcanism. *Journal of African Earth Sciences, 170,* Article ID: 103832. https://doi.org/10.1016/j.jafrearsci.2020.103832

Fitton, J. G. (1987). The Cameroon Line, West Africa: A Comparison between Oceanic and Continental Alkaline Volcanism. *Geological Society, London, Special Publications, 30,* 273-291. https://doi.org/10.1144/gsl.sp.1987.030.01.13

Fosso, J., Ménard, J., Bardintzeff, J., Wandji, P., Tchoua, F. M., & Bellon, H. (2005). Les laves du mont Bangou: Une première manifestation volcanique éocène, à affinité transitionnelle, de la Ligne du Cameroun. *Comptes Rendus. Géoscience, 337,* 315-325. https://doi.org/10.1016/j.crte.2004.10.014

Gawlick, H., Aubrecht, R., Schlagintweit, F., Missoni, S., & Plašienka, D. (2015). Ophiolitic Detritus in Kimmeridgian Resedimented Limestones and Its Provenance from an Eroded Obducted Ophiolitic Nappe Stack South of the Northern Calcareous Alps (Austria). *Geologica Carpathica, 66,* 473-487. https://doi.org/10.1515/geoca-2015-0039

Ge, X. Y., Li, X. H., Chen, Z. G., & Li, W. P. (2002). Geochemistry and Petrogenesis of Jurassic High Sr/low Y Granitoids in Eastern China: Constrains on Crustal Thickness. *Chinese Science Bulletin, 47,* 962-968. https://doi.org/10.1360/02tb9216

Goldstein, S. B., & Francis, D. (2008). The Petrogenesis and Mantle Source of Archaean Ferropicrites from the Western Superior Province, Ontario, Canada. *Journal of Petrology, 49,* 1729-1753. https://doi.org/10.1093/petrology/egn044

Halliday, A. N., Lee, D., Tommasini, S., Davies, G. R., Paslick, C. R., Godfrey Fitton, J. et al. (1995). Incompatible Trace Elements in OIB and MORB and Source Enrichment in the Sub-Oceanic Mantle. *Earth and Planetary Science Letters, 133,* 379-395. https://doi.org/10.1016/0012-821x(95)00097-v

Hart, W. K., WoldeGabriel, G., Walter, R. C., & Mertzman, S. A. (1989). Basaltic Volcanism in Ethiopia: Constraints on Continental Rifting and Mantle Interactions. *Journal of Geophysical Research: Solid Earth, 94,* 7731-7748. https://doi.org/10.1029/jb094ib06p07731

Herzberg, C., & Asimow, P. D. (2008). Petrology of Some Oceanic Island Basalts: PRIMELT2.XLS Software for Primary Magma Calculation. *Geochemistry, Geophysics, Geosystems, 9,* 1-25. https://doi.org/10.1029/2008gc002057

Jankovics, M. É., Dobosi, G., Embey-Isztin, A., Kiss, B., Sági, T., Harangi, S. et al. (2013). Origin and Ascent History of Unusually Crystal-Rich Alkaline Basaltic Magmas from the Western Pannonian Basin. *Bulletin of Volcanology, 75,* Article No. 749. https://doi.org/10.1007/s00445-013-0749-7

Jung, S., & Masberg, P. (1998). Major- and Trace-Element Systematics and Isotope Geochemistry of Cenozoic Mafic Volcanic Rocks from the Vogelsberg (Central Germany): Constraints on the Origin of Continental Alkaline and Tholeiitic Basalts and Their Mantle Sources. *Journal of Volcanology and Geothermal Research, 86,* 151-177. https://doi.org/10.1016/s0377-0273(98)00087-0

Kagou, D. A, Wandji, P., Pouclet, A., Vicat, J., Cheilletz, A., Nkouathio, D. G. et al. (2001). Évolution volcanologique du mont Manengouba (Ligne du Cameroun); nouvelles données pétrographiques, géochimiques et géochronologiques. *Comptes Rendus de l'Académie des Sciences—Series IIA—Earth and Planetary Science, 333,* 155-162. https://doi.org/10.1016/s1251-8050(01)01625-1

Kamgang, P., Chazot, G., Njonfang, E., Ngongang, N. B. T., & Tchoua, F. M. (2013). Mantle Sources and Magma Evolution beneath the Cameroon Volcanic Line: Geochemistry of Mafic Rocks from the Bamenda Mountains (NW Cameroon). *Gondwana Research, 24,* 727-741. https://doi.org/10.1016/j.gr.2012.11.009

Kamgang, P., Njonfang, E., Nono, A., Dedzo, M. G., & Tchoua, F. M. (2010). Petrogenesis of a Silicic Magma System: Geochemical Evidence from Bamenda Mountains, NW Cameroon, Cameroon Volcanic Line. *Journal of African Earth Sciences, 58,* 285-304. https://doi.org/10.1016/j.jafrearsci.2010.03.008

Kawabata, H., Hanyu, T., Chang, Q., Kimura, J., Nichols, A. R. L., & Tatsumi, Y. (2011). The Petrology and Geochemistry of St. Helena Alkali Basalts: Evaluation of the Oceanic

Crust-Recycling Model for HIMU OIB. *Journal of Petrology, 52,* 791-838. https://doi.org/10.1093/petrology/egr003

Keller, B., & Schoene, B. (2018). Plate Tectonics and Continental Basaltic Geochemistry Throughout Earth History. *Earth and Planetary Science Letters, 481,* 290-304. https://doi.org/10.1016/j.epsl.2017.10.031

Kouepou, G., Tchouankoue, J. P., Nagao, T., & Sato, H. (2006). Transitional Tholeiitic Basalts in the Tertiary Bana Volcano-Plutonic Complex, Cameroon Line. *Journal of African Earth Sciences, 45,* 318-332. https://doi.org/10.1016/j.jafrearsci.2006.03.005

Laridhi-Ouazaa, N. (1989). Principales caratéristiques géochimiques des laves basiques miocènes de la Tunisie septentrionale: Nefza et Mogod. *Comptes rendus de l'Académie des Sciences, 308,* 1055-1060.

Le Bas, M. J., Maitre, R. W. L., Streckeisen, A., & Zanettin, B. (1986). A Chemical Classification of Volcanic Rocks Based on the Total Alkali-Silica Diagram. *Journal of Petrology, 27,* 745-750. https://doi.org/10.1093/petrology/27.3.745

Le Maitre, R. W. (2002). *Igneous Rocks: A Classification and Glossary of Terms: Recommendations of the International Union of Geological Sciences Subcommission on the Systematics of Igneous Rocks.* Cambridge University Press.

Marzoli, A., Renne, P. R., Piccirillo, E. M., Francesca, C., Bellieni, G., Melfi, A. J. et al. (1999). Silicic Magmas from the Continental Cameroon Volcanic Line (Oku, Bambouto and Ngaoundere): ^{40}Ar-^{39}Ar Dates, Petrology, Sr-Nd-O Isotopes and Their Petrogenetic Significance. *Contributions to Mineralogy and Petrology, 135,* 133-150. https://doi.org/10.1007/s004100050502

Morimoto, N., Fabries, J., Ferguson, A. K., Ginzburg, I. V., Ross, M., Seifert, F. A. et al. (1988). Nomenclature of Pyroxenes. *Mineralogical Magazine, 52,* 535-550. https://doi.org/10.1180/minmag.1988.052.367.15

Neave, D. A., & Putirka, K. D. (2017). A New Clinopyroxene-Liquid Barometer, and Implications for Magma Storage Pressures under Icelandic Rift Zones. *American Mineralogist, 102,* 777-794. https://doi.org/10.2138/am-2017-5968

Ngako, V., Jegouzo, P., & Nzenti, J. P. (1992). Champ de raccourcissement et de cratonisation du Nord-Cameroun du paléozoïque supérieur au paléozoïque moyen. *Comptes Rendus Académie des Sciences (Paris), 315,* 457-463.

Ngwa, C. N., Hansteen, T. H., Devey, C. W., van der Zwan, F. M., & Suh, C. E. (2017). Origin and Evolution of Primitive Melts from the Debunscha Maar, Cameroon: Consequences for Mantle Source Heterogeneity within the Cameroon Volcanic Line. *Lithos, 288,* 326-337. https://doi.org/10.1016/j.lithos.2017.06.028

Nimis, P. (1999). Clinopyroxene Geobarometry of Magmatic Rocks. Part 2. Structural Geobarometers for Basic to Acid, Tholeiitic and Mildly Alkaline Magmatic Systems. *Contributions to Mineralogy and Petrology, 135,* 62-74. https://doi.org/10.1007/s004100050498

Nimis, P., & Ulmer, P. (1998). Clinopyroxene Geobarometry of Magmatic Rocks Part 1: An Expanded Structural Geobarometer for Anhydrous and Hydrous, Basic and Ultrabasic Systems. *Contributions to Mineralogy and Petrology, 133,* 122-135. https://doi.org/10.1007/s004100050442

Nisbet, E. G., & Pearce, J. A. (1977). Clinopyroxene Composition in Mafic Lavas from Different Tectonic Settings. *Contributions to Mineralogy and Petrology, 63,* 149-160. https://doi.org/10.1007/bf00398776

Niu, Y. (2005). Generation and Evolution of Basaltic Magmas: Some Basic Concepts and a New View on the Origin of Mesozoic-Cenozoic Basaltic Volcanism in Eastern China.

Geological Journal of China Universities, 11, 9-46.

Njonfang, E., Tchoneng, G. T., Cozzupoli, D., & Lucci, F. (2013). Petrogenesis of the Sabongari Alkaline Complex, Cameroon Line (Central Africa): Preliminary Petrological and Geochemical Constraints. *Journal of African Earth Sciences, 83,* 25-54. https://doi.org/10.1016/j.jafrearsci.2013.03.004

Nkouandou, O. F., Bardintzeff, J. M., Mefire, F., Ndassa, N., Sahabo, A. A., & Adama, H. (2023). Petrology of Lherzolite Xenoliths of Hosséré Sédé volcano (Adamawa Plateau, Ngaoundéré Area, Cameroon). *Acta Geochimica, 42,* 817-831. https://doi.org/10.1007/s11631-023-00621-x

Nkouandou, O. F., Mefire, A. F., & Deruelle, B. (2010). Petrogenesis Modeling of the Alkaline Volcanism of Ngaoundéré (Adamawa Plateau, Cameroon, Central Africa). *International Journal of Biological and Chemical Sciences, 10,* 1903-1917. https://doi.org/10.4314/ijbcs.v10i4.38

Nkouandou, O. F., Ngounouno, I., Déruelle, B., Ohnenstetter, D., Montigny, R., & Demaiffe, D. (2008). Petrology of the Mio-Pliocene Volcanism to the North and East of Ngaoundéré (Adamawa, Cameroon). *Comptes Rendus. Géoscience, 340,* 28-37. https://doi.org/10.1016/j.crte.2007.10.012

Onana François Xavier, M., Robert, T., Wagsong Merlin Patrick, N., Gilles, C., Feudjio Anicet, T., Lucas, M. et al. (2022). Petrography, Mineral Chemistry and Geochemistry of Quaternary Volcanism from Wakwa Plain, Adamawa Massif (Cameroon Volcanic Line, West-Central Africa). *Arabian Journal of Geosciences, 15,* Article No. 1106. https://doi.org/10.1007/s12517-022-10279-z

Pearce, J. A. (1996). A User's Guide to Basalt Discrimination Diagrams. In D. A. Wyman (Ed.), *Trace Element Geochemistry of Volcanic Rocks: Applications for Massive Sulphide Exploration* (pp. 79-113). Geological Association of Canada.

Poldervaart, A., & Hess, H. H. (1951). Pyroxenes in the Crystallization of Basaltic Magma. *The Journal of Geology, 59,* 472-489. https://doi.org/10.1086/625891

Poudjom Djomani, Y. H., Nnange, J. M., Diament, M., Ebinger, C. J., & Fairhead, J. D. (1995). Effective Elastic Thickness and Crustal Thickness Variations in West Central Africa Inferred from Gravity Data. *Journal of Geophysical Research: Solid Earth, 100,* 22047-22070. https://doi.org/10.1029/95jb01149

Roeder, P. L., & Emslie, R. F. (1970). Olivine-liquid equilibrium. *Contributions to Mineralogy and Petrology, 29,* 275-289. https://doi.org/10.1007/bf00371276

Sato, H., Aramaki, S., Kusakabe, M., Hirabayashi, J., Sano, Y., Nojiri, Y. et al. (1990). Geochemical Difference of Basalts between Polygenetic and Monogenetic Volcanoes in the Central Part of the Cameroon Volcanic Line. *Geochemical Journal, 24,* 357-370. https://doi.org/10.2343/geochemj.24.357

Schweitzer, E. L., Papike, J. J., & Bence, A. E. (1979). Statistical Analysis of Clinopyroxenes from Deep Sea Basalts. *American Mineralogist, 64,* 501-513.

Smith, E. I., Sánchez, A., Walker, J. D., & Wang, K. (1999). Geochemistry of Mafic Magmas in the Hurricane Volcanic Field, Utah: Implications for Small- and Large-Scale Chemical Variability of the Lithospheric Mantle. *The Journal of Geology, 107,* 433-448. https://doi.org/10.1086/314355

Suh, C. E., Luhr, J. F., & Njome, M. S. (2008). Olivine-Hosted Glass Inclusions from Scoriae Erupted in 1954-2000 at Mount Cameroon Volcano, West Africa. *Journal of Volcanology and Geothermal Research, 169,* 1-33. https://doi.org/10.1016/j.jvolgeores.2007.07.004

Sun, S. S., & McDonough, W. F. (1989). Chemical and Isotopic Systematics of Oceanic

Basalts: Implications for Mantle Composition and Processes. *Geological Society, London, Special Publications, 42,* 313-345. https://doi.org/10.1144/gsl.sp.1989.042.01.19

Tamen, J., Nkoumbou, C., Mouafo, L., Reusser, E., & Tchoua, F. M. (2007). Petrology and Geochemistry of Monogenetic Volcanoes of the Barombi Koto Volcanic Field (Kumba Graben, Cameroon Volcanic Line): Implications for Mantle Source Characteristics. *Comptes Rendus. Géoscience, 339,* 799-809. https://doi.org/10.1016/j.crte.2007.09.007

Tamen, J., Nkoumbou, C., Reusser, E., & Tchoua, F. (2015). Petrology and Geochemistry of Mantle Xenoliths from the Kapsiki Plateau (Cameroon Volcanic Line): Implications for Lithospheric Upwelling. *Journal of African Earth Sciences, 101,* 119-134. https://doi.org/10.1016/j.jafrearsci.2014.09.008

Tanyileke, G. Z., Kusakabe, M., & Evans, W. C. (1996). Chemical and Isotopic Characteristics of Fluids along the Cameroon Volcanic Line, Cameroon. *Journal of African Earth Sciences, 22,* 433-441. https://doi.org/10.1016/0899-5362(96)00025-5

Tatsumi, Y., Sakuyama, M., Fukuyama, H., & Kushiro, I. (1983). Generation of Arc Basalt Magmas and Thermal Structure of the Mantle Wedge in Subduction Zones. *Journal of Geophysical Research: Solid Earth, 88,* 5815-5825. https://doi.org/10.1029/jb088ib07p05815

Tchameni, R., Pouclet, A., Penaye, J., Ganwa, A. A., & Toteu, S. F. (2006). Petrography and Geochemistry of the Ngaoundéré Pan-African Granitoids in Central North Cameroon: Implications for Their Sources and Geological Setting. *Journal of African Earth Sciences, 44,* 511-529. https://doi.org/10.1016/j.jafrearsci.2005.11.017

Temdjim, R., Tchouankoue, J. P., & Tchoua, F. (2006). On Existence of a Trachytic Maar in the Cameroon Volcanic Line: Mbalang-Djalingo Maar in Ngaoundéré Region (Adamawa Plateau). *Revue de geographie du Cameroun, XVII,* 67-71.

Thompson, J. P. (1947). Role of Aluminium in Rock Forming Silicates. *Bulletin Society American, 58,* 1232.

Tiabou, A. F., Temdjim, R., Wandji, P., Bardintzeff, J., Che, V. B., Bate Tibang, E. E. et al. (2018). Baossi-Warack Monogenetic Volcanoes, Adamawa Plateau, Cameroon: Petrography, Mineralogy and Geochemistry. *Acta Geochimica, 38,* 40-67. https://doi.org/10.1007/s11631-018-0272-9

Tsafack, J. P. F., Wandji, P., Bardintzeff, J. M., Bellon, H., & Guillou, H. (2009). The Mount Cameroon Stratovolcano (Cameroon Volcanic Line, Central Africa): Petrology, Geochemistry, Isotope and Age Data. *Geochemistry, Mineralogy and Petrology, 47,* 65-78.

Wass, S. Y. (1979). Multiple Origins of Clinopyroxenes in Alkali Basaltic Rocks. *Lithos, 12,* 115-132. https://doi.org/10.1016/0024-4937(79)90043-4

Weaver, B. L. (1991). The Origin of Ocean Island Basalt End-Member Compositions: Trace Element and Isotopic Constraints. *Earth and Planetary Science Letters, 104,* 381-397. https://doi.org/10.1016/0012-821x(91)90217-6

Weaver, B. L., Wood, D. A., Tarney, J., & Joron, J. L. (1987). Geochemistry of Ocean Island Basalts from the South Atlantic: Ascension, Bouvet, St. Helena, Gough and Tristan Da Cunha. *Geological Society, London, Special Publications, 30,* 253-267. https://doi.org/10.1144/gsl.sp.1987.030.01.11

Wembenyui, E. W., Collerson, K. D., & Zhao, J. (2020). Evolution of Mount Cameroon Volcanism: Geochemistry, Mineral Chemistry and Radiogenic Isotopes (Pb, Sr, Nd). *Geoscience Frontiers, 11,* 2157-2168. https://doi.org/10.1016/j.gsf.2020.03.015

Wilson, M. (1992). Magmatism and Continental Rifting during the Opening of the South Atlantic Ocean: A Consequence of Lower Cretaceous Super-Plume Activity? *Geological Society, London, Special Publications, 68,* 241-255. https://doi.org/10.1144/gsl.sp.1992.068.01.15

Yang, Z., & Zhou, J. (2013). Can We Identify Source Lithology of Basalt? *Scientific Reports, 3,* Article No. 1856. https://doi.org/10.1038/srep01856

Yokoyama, T., Aka, F. T., Kusakabe, M., & Nakamura, E. (2007). Plume-Lithosphere Interaction Beneath Mt. Cameroon Volcano, West Africa: Constraints from ^{238}U-^{230}Th-^{226}Ra and Sr-Nd-Pb Isotope Systematics. *Geochimica et Cosmochimica Acta, 71,* 1835-1854. https://doi.org/10.1016/j.gca.2007.01.010

Yuan, L., Yan, Q., Liu, Y., Wu, S., Wang, R., & Shi, X. (2020). *In Situ* Geochemical Compositions of the Minerals in Basaltic Rocks from the West Philippine Basin: Constraints on Source Lithology and Magmatic Processes. *Lithosphere, 2020,* Article ID: 8878501. https://doi.org/10.2113/2020/8878501